Article

Effect of Adding Chelating Ligands on the Catalytic Performance of Rh-Promoted MoS₂ in the Hydrodesulfurization of Dibenzothiophene

Siphumelele Majodina *, Zenixole R. Tshentu (ID) **and Adeniyi S. Ogunlaja *** (ID)

Department of Chemistry, Nelson Mandela University, P.O. Box 77000, Gqeberha 6031, South Africa;
Zenixole.Tshentu@mandela.ac.za
* Correspondence: s217553532@mandela.ac.za (S.M.); Adeniyi.Ogunlaja@mandela.ac.za (A.S.O.)

Abstract: Hydrodesulfurization (HDS) is a widely used process currently employed in petroleum refineries to eliminate organosulfur compounds in fuels. The current hydrotreating process struggles to remove organosulfur compounds with a steric hindrance due to the electronic nature of the current catalysts employed. In this work, the effects of adding chelating ligands such as ethylenediaminetetraacetic acid (EDTA), citric acid (CA) and acetic acid (AA) to rhodium (Rh) and active molybdenum (Mo) species for dibenzothiophene (DBT) HDS catalytic activity was evaluated. HDS activities followed the order of RhMo/ɣ-Al₂O₃ (88%) > RhMo-AA/ɣ-Al₂O₃ (73%) > RhMo-CA/ɣ-Al₂O₃ (72%) > RhMo-EDTA/ɣ-Al₂O₃ (68%). The observed trend was attributed to the different chelating ligands with varying electronic properties, thus influencing the metal–support interaction and the favorable reduction of the Mo species. RhMo/ɣ-Al₂O₃ offered the highest HDS activity due to its (i) lower metal–support interaction energy, as observed from the RhMo/ɣ-Al₂O₃ band gap of 3.779 eV and the slight shift toward the lower BE of Mo 3d, (ii) increased Mo-O-Mo species ($N_{Mo-O-Mo}$ ~1.975) and (iii) better sulfidation of Rh and MoO in RhMo/ɣ-Al₂O₃ compared to the chelated catalysts. The obtained data provides that HDS catalytic activity was mainly driven by the structural nature of the RhMo-based catalyst, which influences the formation of more active sites that can enhance the HDS activity.

Keywords: hydrodesulfurization (HDS); chelating ligands; molybdenum disulfide (MoS₂); dibenzothiophene; RhMo-(L)-γ-Al₂O₃

1. Introduction

Deleterious refractory organosulfur compounds in fuel oils have contributed to SOx emissions [1,2]. Therefore, it has become very important to remove these compounds due to the introduction of the strict environmental regulations of the Euro V limits of 10 ppmS in diesel fuels [1,2].

Hydrodesulfurization (HDS) is the most commonly used technology to produce clean fuels by employing hydrotreating catalysts, mainly from Co(Ni)/Mo oxides supported on alumina [3–11]. The production of ultra-low fuels using the HDS process at present requires extreme and expensive operating conditions, viz., high temperatures, hydrogen and highly active catalysts.

However, other methods of fuel desulfurization have been reported, and these techniques are bio-desulfurization (BDS), oxidative-desulfurization (ODS), adsorptive and extractive desulfurization (ADS and EDS) [1,2]. Bio-desulfurization (BDS), which involves the use of sulfur-consuming bacteria to desulfurize fuels, is nonetheless limited in meeting very deep desulfurization, as 50–200 ppmS have been reported [1]. The ODS process of recalcitrant sulfur-containing compounds such as dibenzothiophene have been reported to produce nonessential side products during oxidation [2]. Adsorptive and extractive desulfurization (ADS and EDS) is a process which employs the use of use of solid sorbents

and extraction solvents for removing the recalcitrant sulfur-containing compounds, respectively. Adsorbents have been limited in organosulfur compound selectivity, as well as low adsorption capacity, while the organosulfur extraction solvents such as dimethylsulfoxide (DMSO) and *N,N*-dimethylformamide (DMF) have high boiling points, and hence the solvent recovery may be impossible [1,2]. The use of ODS, BDS, ADS and EDS desulfurization techniques are currently limited, as they may pose problems for larger scale applications [1,2]. As a result, more attention is required to improve the HDS system by redesigning the current HDS catalysts' inadequacies and by introducing chelating ligands and precious metals (PGMs), which could drive HDS under mild conditions [3–26].

Several transition metal sulfides have been reported as possible candidates for the HDS catalysts [15–30]. Rhodium-based catalysts have exhibited promising properties, hence showing great potential as an HDS catalyst. A few HDS studies of dibenzothiophene (DBT) over Rh-based catalysts have been reported. Lee et al. [27] reported that the RhCs/Al$_2$O$_3$ catalyst was more active than a conventional CoMo/Al$_2$O$_3$ catalyst for hydrotreating dibenzothiophene. RhCs/Al$_2$O$_3$-catalyzed DBT hydrodesulfurization was mainly controlled by the DDS (direct desulfurization) mechanism. Similarly, a synergetic effect was reported with the RhMo/ɣ-Al$_2$O$_3$ catalysts, suggesting that Rh and Mo interact when employed for DBT HDS [28]. While there are reports on the use of RhMo-based catalysts [27,28], studies with regards to the influence of chelating ligands, especially acetic acid (AA), on hydrotreating activity is lacking. Chelating ligands are molecules with two or more donor atoms available to bind a metal cation, and they have been reported to improve hydrotreating activity [15,17,29–31].

The scientific novelty of the research is to arrive at a fundamental understanding of the nature of the sulfur tolerance of the supported Rh-Mo catalysts (chelated and unchelated RhMoS/ɣ-Al$_2$O$_3$), and to offer clarification of the synergetic effect of chelating ligands such as ethylenediaminetetraacetic acid (EDTA), citric acid (CA) and acetic acid (AA) on the individual metal, the Rh and the Mo components in the catalytic hydrodesulfurization of DBT. The originality of the research was in the design and the application of the nanostructured RhMo catalysts in the presence of the chelating ligands so to ensure the uniform composition of the catalytic metal species for ease of physico-chemical characterization and the fundamental understanding of the structure-activity relationships. In this study, the HDS catalytic activity of the RhMo-based catalysts were carried out on dibenzothiophene (DBT). The as-synthesized catalysts were characterized using powder X-ray diffraction (PXRD), ultraviolet-visible diffuse reflectance spectroscopy (UV-vis DRS), Fourier transform infrared spectroscopy (FT-IR), scanning electron microscope (SEM), energy-dispersive X-ray spectroscopy (EDX), X-ray photoelectron spectroscopy (XPS), transmission electron microscopes (TEM) and thermogravimetric analysis (TGA)—differential scanning calorimetry (DSC) (TGA-DSC) to determine the catalysts' bulk chemical compositions, morphologies and thermal stability.

The main findings are as follows:

(1) The prepared catalysts presented band gaps of 3.779 eV (RhMo/ɣ-Al$_2$O$_3$), 4.341 eV (RhMo-EDTA/ɣ-Al$_2$O$_3$), 4.394 eV (RhMo-AA/ɣ-Al$_2$O$_3$) and 4.478 eV (RhMo-CA/ɣ-Al$_2$O$_3$), respectively.

(2) The introduction of different chelating ligands increases the metal–support interaction, which prevents the formation of easily reduced Mo species.

(3) The HDS activity decreased in the following order: RhMo/ɣ-Al$_2$O$_3$ (88%) > RhMo-AA/ɣ-Al$_2$O$_3$ (73%) > RhMo-CA/ɣ-Al$_2$O$_3$ (72%) > RhMo-EDTA/ɣ-Al$_2$O$_3$ (68%).

(4) The observed catalytic results were ascribed to the introduction of different ligands, thus increasing the metal–support interaction and increasing the e-charge transfer from the valance band Rh 4d orbital to the conduction band of the Mo species. This led to the excessive weakening of the Mo-S bond by inhibiting the absorption of sulfur (S) compound (DBT) on the active sites, hence leading to a reduced activity.

2. Results and Discussion

2.1. UV-Vis Spectroscopy

UV-vis spectroscopy was applied to study RhMo/γ-Al$_2$O$_3$, RhMo-EDTA/γ-Al$_2$O$_3$ and RhMo-CA/γ-Al$_2$O$_3$, and are shown in Figure 1. As shown in Figure 1, the UV-vis spectra recorded for RhMo/γ-Al$_2$O$_3$ and RhMo(x)/γ-Al$_2$O$_3$ (x = EDTA, CA and AA) exhibited a broad absorption band at 210–290 nm and were assigned to the O^{2-}→Mo^{6+} ligand–metal charge transfer transitions in an octahedral environment [32]. A weak band observed in the region of 340–360 nm with RhMo/γ-Al$_2$O$_3$ was associated with Rh(III) oxides, and another weak broad band at a visible region displayed at 452 nm was due to the presence of Rh(III) in oxide form [33]. A weak absorbance at 530 nm provided strong evidence of well-dispersed octahedral Rh oxide species [34,35], which are known to be easily reduced and sulfided [36–38]. A band around 550–680 nm on RhMo/γ-Al$_2$O$_3$ was due to Rh^{3+} interacting with γ-Al$_2$O$_3$ support to form a rhodium aluminate complex [32]. With the addition of the ligands, the absorbance of Rh^{3+} shifts, as do the weak broad bands around 430 nm, 410–470 nm and 420 nm associated with the metal to ligand transfer, and Rh-O species for RhMo-AA/γ-Al$_2$O$_3$, RhMo-EDTA/γ-Al$_2$O$_3$ and RhMo-CA/γ-Al$_2$O$_3$ were observed. The observed shifts to the lower wavelength suggested that the Rh–ligand complexes inhibit the formation of the Rh-γ-Al$_2$O$_3$ phase [32,39]. The shift to a lower wavelength also indicated a decreased agglomeration of the Mo species [32,40,41].
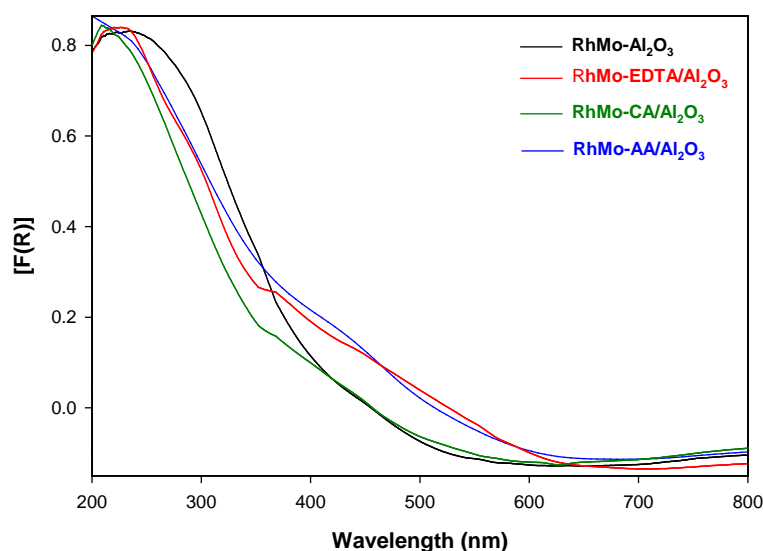
Figure 1. UV-vis spectra of RhMo/Al$_2$O$_3$ and RhMo-x/γ-Al$_2$O$_3$ (x = EDTA, AA, CA) catalysts.

2.2. Band Gaps of RhMo Catalysts

The E$_g$ value obtained from the Tauc and Davis–Mott Equation (1) demonstrates the dispersion of the Mo species. The band gaps for RhMo/γ-Al$_2$O$_3$, RhMo-EDTA/γ-Al$_2$O$_3$, RhMo-CA/γ-Al$_2$O$_3$ and RhMo-AA/Al$_2$O$_3$ were determined and are displayed in Figure S1. According to the literature, the higher the E$_g$ value, the more improved the dispersion of the Mo species [42]. The obtained band gap for RhMo/Al$_2$O$_3$ was 3.779 eV (Figure S1), the E$_g$ value obtained for RhMo-EDTA/γ-Al$_2$O$_3$ was 4.341 eV, the E$_g$ value RhMo-AA/γ-Al$_2$O$_3$ was E$_g$ = 4.394 eV and the E$_g$ value for RhMo-CA/γ-Al$_2$O$_3$ was 4.478 eV. The RhMo-CA/γ-Al$_2$O$_3$ catalyst exhibited the highest E$_g$ value, which implies a decrease in the average particle size and an increased charge transfer [41–44].

$$(\alpha h\nu)^{\frac{1}{n}} = A\left(h\nu - E_g\right) \tag{1}$$

where α is the absorption coefficient, $h\nu$ is the incident photon energy, A is the proportionality constant, E$_g$ is the optical band gap energy and n represents the nature of the electronic transition (n = 1/2 for direct transition).

The bridging Mo-O-Mo bonds, which determine the degree of polymerization/aggregation of Mo(VI), were determined from the E_g values by using the formula ($N_{Mo-O-Mo} = 11.8 - 26E_g$) presented by Tian et al. (2010) [42]. It was established that the higher E_g values of the catalysts corresponded to the lower average number (of covalent bridging of the central Mo^{6+} cation) nearest to the Mo^{6+} neighbours (Table 1), thus confirming the Mo(VI) cation structural variations in the catalysts. RhMo/γ-Al$_2$O$_3$ was reported to offer more polymeric/aggregated Mo species compared to the chelated catalysts (RhMo-AA/γ-Al$_2$O$_3$, RhMo-EDTA/γ-Al$_2$O$_3$ and RhMo-CA/γ-Al$_2$O$_3$).

Table 1. Band gap energy and average number of nearest Mo^{6+} neighbors ($N_{Mo-O-Mo}$) in deposited clusters, as determined from UV spectra of the oxide RhMo catalysts.

Catalyst	E_g Values	$N_{Mo-O-Mo}$
RhMo/γ-Al$_2$O$_3$	3.779	1.975
RhMo-AA/γ-Al$_2$O$_3$	4.341	0.5134
RhMo-EDTA/γ-Al$_2$O$_3$	4.394	0.3756
RhMo-CA/γ-Al$_2$O$_3$	4.478	0.1572

$N_{Mo-O-Mo}$ = 11.8–2.6E_g.

2.3. Fourier Transform Infrared Spectroscopy (FT-IR)

FT-IR bands at 3600–2800 cm^{-1} correspond to the OH (from H$_2$O) stretching. At the region between 550 cm^{-1}, the corresponding band was assigned to the Mo-O-Mo bridge stretching, while the bands that were found, and the Mo=O stretching, were located at 950 cm^{-1} [45]. RhMo-EDTA/Al$_2$O$_3$ showed an absorption band at 978 cm^{-1}, which could be assigned to the Mo-N band [35,45]. At 1588 cm^{-1}, the absorption band could be assigned to -COO$^-$ vibrations with H$_2$O [46] (Figure S2).

2.4. Energy Dispersion Spectroscopy (EDX)

The EDS of the sulfided RhMo/Al$_2$O$_3$, RhMo-EDTA/Al$_2$O$_3$, RhMo-AA/Al$_2$O$_3$ and RhMo-CA/Al$_2$O$_3$ catalysts confirmed that the catalysts are made up of Rh, Mo, O, S, C and Al (Figure S3). The peaks at ~2.37, ~2.7, ~2.81 and ~3.28 KeV corresponded to the theoretical L_α, K_α and K_β of Rh, respectively. The peaks at ~2.3 and 2.81 KeV corresponded to the theoretical L_α, K_α and K_β of Mo, and the O peak was obtained at ~0.5 KeV and the S peak at ~2.3 KeV. The additional peak at ~1.5 KeV corresponded to Al from the support, and the presence of carbon (~0.28 KeV) was due to the carbon tape that was used for the sample analysis [47]. Table 2 illustrates the qualitative atomic percentage of the present elements for each HDS catalyst. The S/Mo atomic ratio for the catalysts are around (0.47–4.63) and the amounts of carbon (5.46 $\leq$ C/Mo $\leq$ 31.88) are found in all of the MoS$_2$ catalysts. The main source of carbon is most probably the heptane solvent [48,49].

**Table 2.** Qualitative atomic percentage of Rh, C, O, S and Mo for sulfided HDS catalysts.

Catalysts	Atomic Percentage (wt. %)						S/Mo	C/Mo
	C K	O K	Al K	S K	Rh L	Mo L		
RhMo/γ-Al$_2$O$_3$	7.97	63.24	26.47	0.68	0.17	1.46	0.47	5.46
RhMo-EDTA/γ-Al$_2$O$_3$	10.20	57.52	30.03	1.48	0.44	0.32	4.63	31.88
RhMo-AA/γ-Al$_2$O$_3$	9.38	62.61	25.63	1.35	0.19	0.73	1.85	12.85
RhMo-CA/γ-Al$_2$O$_3$	12.07	57.56	26.88	1.60	0.94	0.90	1.78	13.41

2.5. X-ray Diffraction (XRD)

The XRD analysis was performed to identify the diffraction phases and dispersion of the synthesized RhMo/γ-Al$_2$O$_3$ and RhMo-x/γ-Al$_2$O$_3$ (x = EDTA, acetic acid (AA), citric acid (CA)) catalysts. Figure 2 showed that all of the RhMo catalysts in the oxide phase had similar diffraction patterns at 2θ = 19.6°, 32.0°, 37.6°, 39.5°, 45.5°, 60.9° and

67.0°, and were assigned to (220), (311), (222), (400), (511) and (440), characteristic of the γ-Al$_2$O$_3$ face-centered cubic phase, respectively. For the RhMo/γ-Al$_2$O$_3$ catalyst, more patterns were observed at 2θ = 12.1°, 18.5° and 28.5°, which were due to the orthorhombic MoO$_3$ crystalline phase [50], and the diffraction pattern at 49.0° could be ascribed to the monoclinic crystalline phase of MoO$_3$. The pattern observed at 2θ = 34.1° could be attributed to Rh$_2$O$_3$ phase, and diffraction patterns at 56.0° and 57.8° were also observed. All of the chelated catalysts showed the characteristic reflections of alumina supports and very weak reflection peaks for RhMo-CA/γ-Al$_2$O$_3$, which indicated that the addition of the chelating agent could promote the redispersion of the bulk MoO$_3$ [40,51,52]. The broadness and the amorphous nature of the diffraction pattern observed in the chelated catalysts indicated the absence of crystalline MoO$_3$ (RhMo-CA/γ-Al$_2$O$_3$). Sulfided RhMo/γ-Al$_2$O$_3$ presented a hexagonal MoS$_2$ phase at 14.8°, 29.5°, 33.3°, 38.5° and 60.4°. According to the obtained result, it was shown that the addition of the chelating ligands resulted in the better dispersion of molybdenum oxide [53]. Additional peaks attributed to the rhodium sulfide phase (Rh$_2$S$_3$ and/or Rh$_3$S$_4$), with characteristic peaks at 2θ = 36–42, were detected on all the sulfided RhMo-x/γ-Al$_2$O$_3$, with RhMo/γ-Al$_2$O$_3$ exhibiting more characteristic peaks compared to RhMo-x/γ-Al$_2$O$_3$. The broad diffraction peaks of the sulfided catalysts (Figure 2b–d) compared to RhMo/γ-Al$_2$O$_3$ (Figure 2a) showed bulk and relatively smaller crystallite sizes. The RhMo catalysts' crystallite sizes decreased in the order of RhMo/γ-Al$_2$O$_3$ (5.903 nm) > RhMo-CA/γ-Al$_2$O$_3$ (5.809 nm) > RhMo-EDTA/γ-Al$_2$O$_3$ (5.770 nm) > RhMo-AA/γ-Al$_2$O$_3$ (5.750 nm).
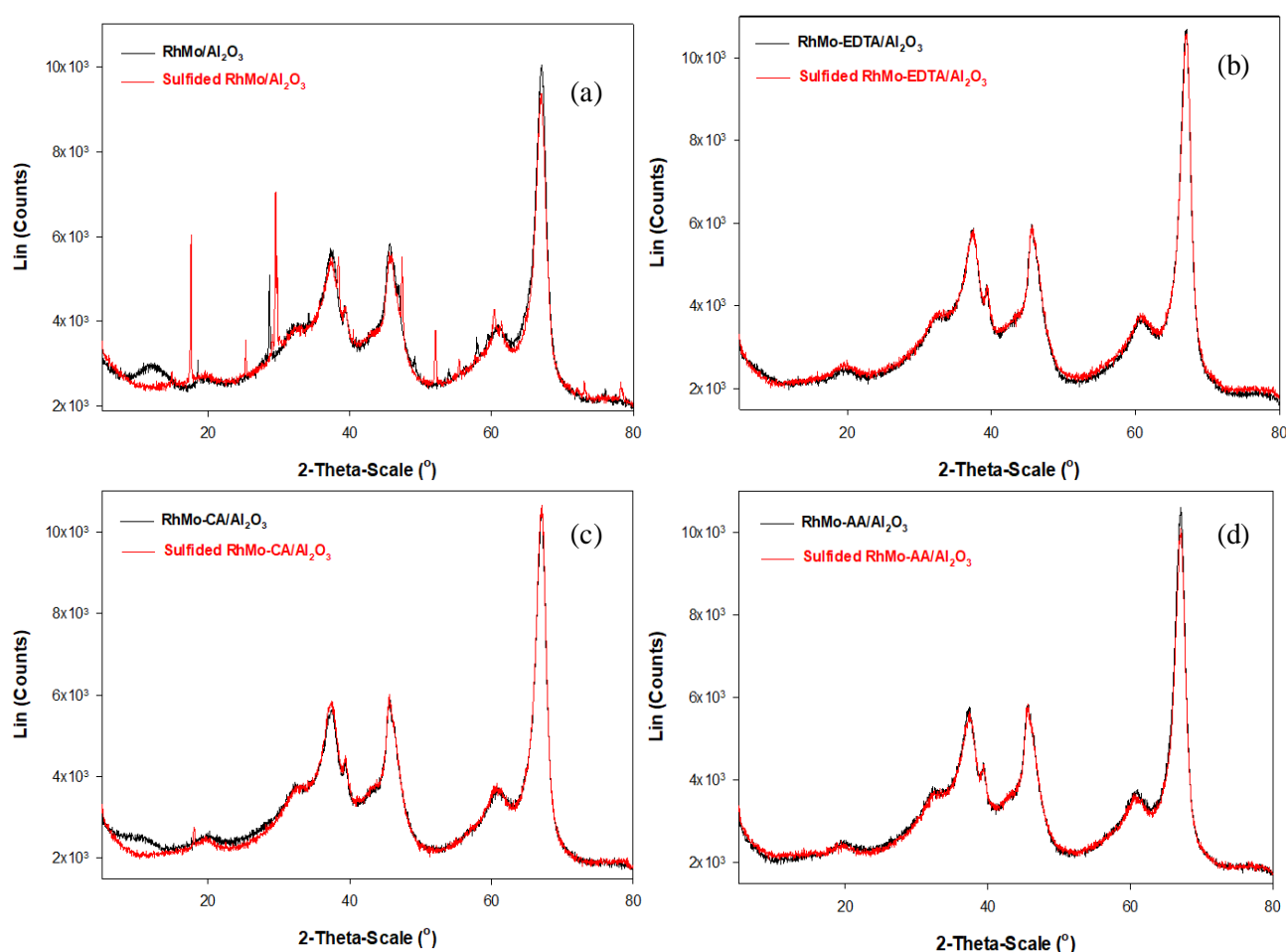
Figure 2. XRD diffraction pattern for oxide and sulfided (**a**) RhMo/γ-Al$_2$O$_3$, (**b**) RhMo-EDTA/γ-Al$_2$O$_3$, (**c**) RhMo-AA/γ-Al$_2$O$_3$, (**d**) RhMo-CA/γ-Al$_2$O$_3$ catalysts.

2.6. XPS Analysis

The XPS survey spectrum of sulfided RhMo/ɣ-Al$_2$O$_3$ and RhMo-EDTA/ɣ-Al$_2$O$_3$ catalysts with the detected species, viz., S 2p, Rh 3d and Mo 3d, are presented in Figures 3 and 4, respectively. The survey scan spectrum, shown in Figures 3a and 4a, demonstrated the presence of the key elements, O 1s, S 2p, C 1s, Al 2p and 2s, Rh 3d and Mo 3d in the catalysts. The highly resolved measurements of these individual elements of O 1s, C 1s, Al 2p, and Al 2s are demonstrated in Figures S3a–d and S4a–d for the RhMo/ɣ-Al$_2$O$_3$ and RhMo-EDTA/ɣ-Al$_2$O$_3$ catalysts. The binding energies of these elements are shown in Table 3, and these energies signify the presence of the elements on the catalysts. The XPS result of the Rh 3d peaks for RhMo/ɣ-Al$_2$O$_3$ showed doublets at the binding energies of 306.5 and 310.6 eV, and for RhMo-EDTA/ɣ-Al$_2$O$_3$, the Rh 3d binding energies were obtained at 305.0 and 310.1 eV, respectively [54,55]. Mo 3d showed three characteristic peaks observed at 226, 230.0, and 233.2 eV for RhMo/ɣ-Al$_2$O$_3$ and two visible peaks at 226 and 230.0 eV for RhMo-EDTA/ɣ-Al$_2$O$_3$, respectively.
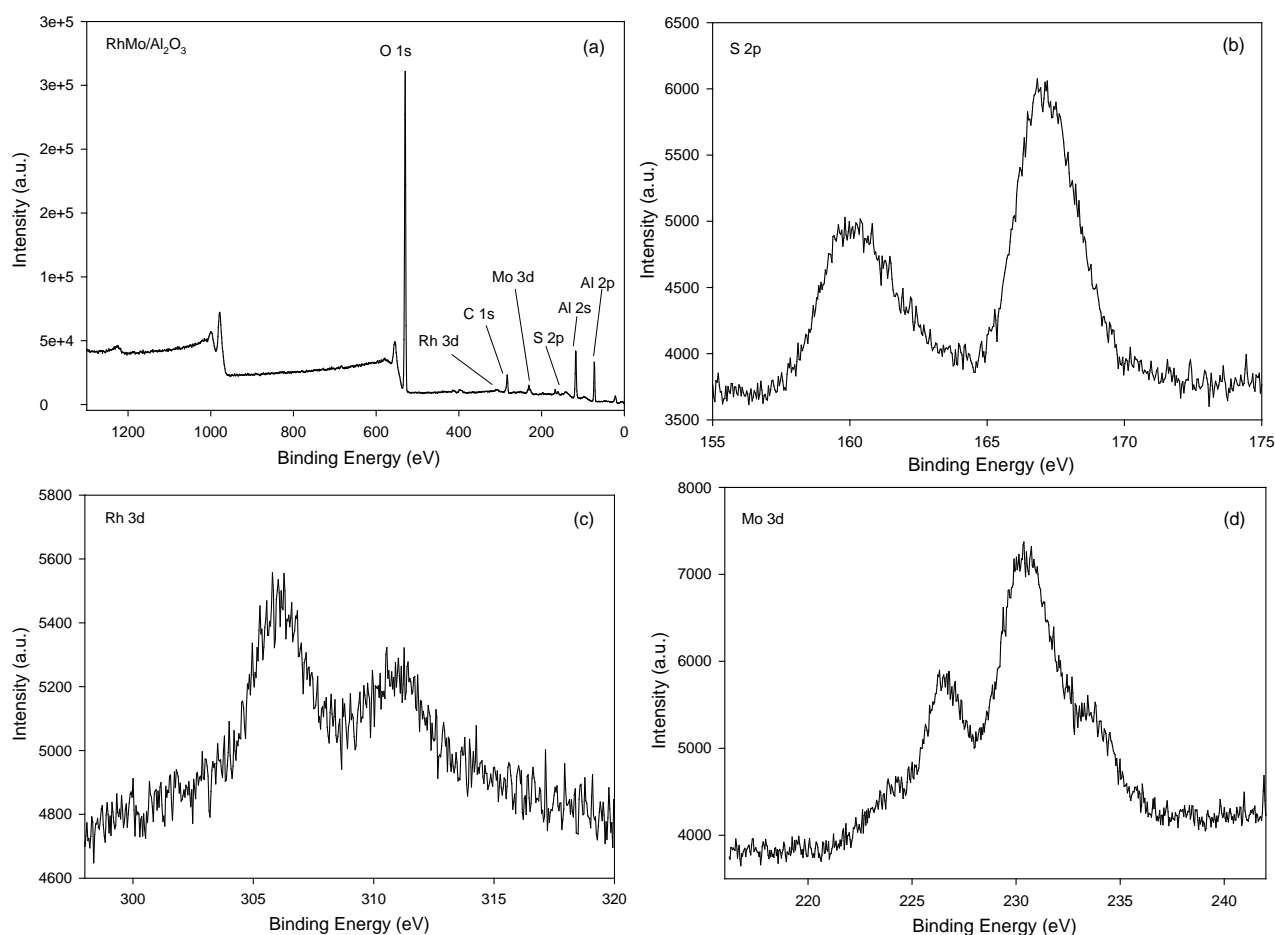
Figure 3. XPS spectra for (**a**) RhMo/ɣ-Al$_2$O$_3$ survey spectrum with different elemental contributions, (**b**) S 2p, (**c**) Rh 3d, (**d**) Mo 3d.

Table 3. Binding energies determined in XPS experiments for RhMo/Al$_2$O$_3$ and RhMo-EDTA/ɣ-Al$_2$O$_3$.

Elements (eV)	RhMo/ɣ-Al$_2$O$_3$	RhMo-EDTA/ɣ-Al$_2$O$_3$
C 1s	289.5	285.5
O 1s	530.0	529.0
Mo 3d	226.2; 230.0; 233.2	226.0; 230.0
Rh 3d	306.5; 310.6	305.0; 310.1

Table 3. *Cont.*

Elements (eV)	RhMo/ɣ-Al$_2$O$_3$	RhMo-EDTA/ɣ-Al$_2$O$_3$
S 2p	160.1; 167.0	160.5; 166.1
Al 2p	72.4	72.0
Al 2s	117.0	117.0
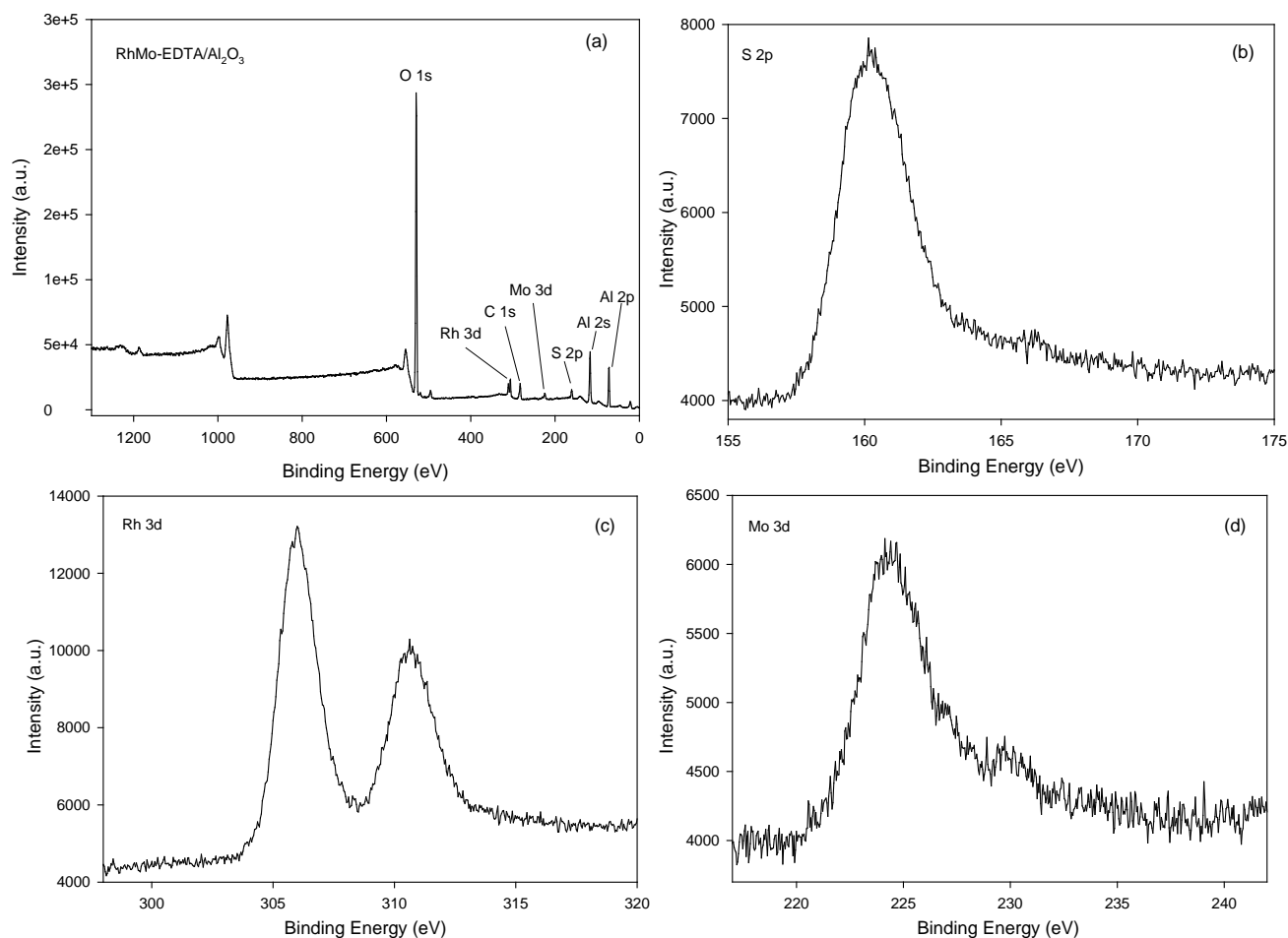
Figure 4. XPS spectra for (**a**) RhMo-EDTA/ɣ-Al$_2$O$_3$ survey spectrum with different elemental contributions, (**b**) S 2p, (**c**) Rh 3d, (**d**) Mo 3d.

To investigate the different phases within the samples for Rh 3d and Mo 3d for the sulfided RhMo/ɣ-Al$_2$O$_3$ and RhMo-EDTA/ɣ-Al$_2$O$_3$, the spectra were carefully deconvoluted and the obtained results are presented in Figure 5a–d. The rhodium oxide (Rh$_2$O$_3$) showed characteristic peaks between 307–310 for Rh 3d$_{5/2}$, and for Rh 3d$_{3/2}$ showed characteristic peaks at a region between 312–315 eV [52,56], and the corresponding results are presented in Figure 5a,c. The Rh$_2$S$_3$ phase showed a doublet at the binding energies of 307–309.2 and 312.7–314 eV in the sulfided RhMo/ɣ-Al$_2$O$_3$ and RhMo-EDTA/ɣ-Al$_2$O$_3$ samples (Table S2), corresponding to the Rh 3d$_{5/2}$ and Rh 3d$_{3/2}$ states for rhodium sulfide, respectively [54–56]. The Mo 3d was comprised of three main peaks with oxidation states of +V (oxide), +V (oxysulfide) and +IV (sulfide) [57,58]. Figure 5b,d shows the deconvolution of the Mo 3d spectra. In the case of Mo, its deconvolution consisted of Mo^{4+} (228.4–229.1 eV, sulfide MoS$_2$), Mo^{5+} (229.7–230.5 eV, oxysulfide MoS$_x$O$_y$) and Mo^{6+} (232.1–232.7 eV, oxide MoO$_3$) [59].
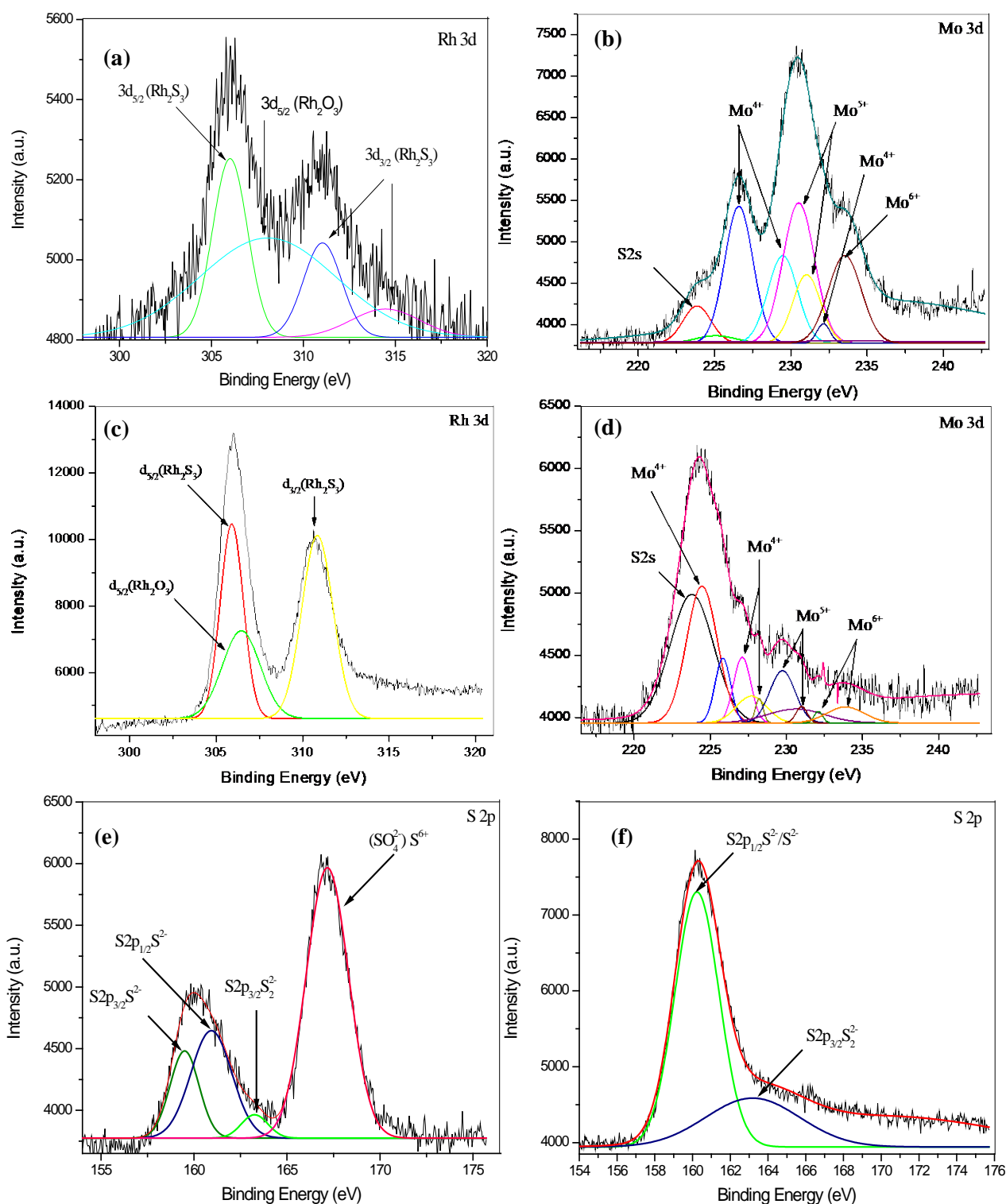
Figure 5. XPS deconvolution of RhMo/ɣ-Al₂O₃ and RhMo-EDTA/ɣ-Al₂O₃, where: (**a**) Rh 3d for RhMo/ɣ-Al₂O₃; (**b**) Mo 3d for RhMo/ɣ-Al₂O₃; (**c**) Rh 3d for RhMo-EDTA/ɣ-Al₂O₃; (**d**) Mo 3d for RhMo-EDTA/ɣ-Al₂O₃; (**e**) S 2p for RhMo/ɣ-Al₂O₃; (**f**) S 2p RhMo-EDTA/ɣ-Al₂O₃.

The doublet at a binding energy (BE) of ($\pm$) 229 eV and ($\pm$) 232.1 0.1 eV was attributed to Mo $3d_{5/2}$ and Mo $3d_{3/2}$ levels of MoS₂ (Mo⁴⁺), and the two contributions observed at ($\pm$) 230.0 eV and ($\pm$) 235.3 0.1 eV were assigned to Mo $3d_{5/2}$ and Mo $3d_{3/2}$ of Mo oxysulfide (MoOₓSᵧ, Mo⁵⁺) [59], while the binding energy of the Mo $3d_{5/2}$ component located at ($\pm$) 232.2 0.1 eV was assigned to the Mo⁶⁺ (MoOₓ) species [60], and for the Mo $3d_{3/2}$

energy level, the binding energy was ($\pm$) 236.0 eV, respectively [61]. The peak presented at 226.3 and 226.1 eV was ascribed to the S 2s level of sulfur (Figure 5e,f). The analysis results, including the detailed binding energies and the sulfidation degree of the Mo species obtained by the deconvolution, are shown in Table S1, and the different phase compositions of the catalysts are calculated from the area of the deconvoluted peaks. Figure 5e,f displays a contribution at 162.1 eV at the lower binding energy of the S 2p peak originating from the S^{2-} precursor [62], and it was clearly visible in both catalysts. The S 2p region suggests the existence of S^{2-}, S_2^{2-} and SO_4^{2-} species [63,64]. The peaks at 162.3 and 163.5 eV are assigned to the S^{2-} in the $2p_{3/2}$ and $2p_{1/2}$ levels, respectively, in MoS_2 [40,51,63,65], and the characteristic peak in S 2p at 166.7 eV was attributed to SO_4^{2-} [66]. The sulfidation degree of the Mo species was calculated by the following Formula (2):

$$\left[Mo^{4+}\right](\%) = \frac{A_{Mo^{4+}}}{A_{Mo^{4+}} + A_{Mo^{5+}} + A_{Mo^{6+}}} \times 100\% \qquad (2)$$

where $[Mo^{4+}]$ is the sulfidation degree of the samples, and A_{Mo}^{4+}, A_{Mo}^{5+} and A_{Mo}^{6+} are the areas of the peaks which are assigned to the Mo^{4+}, Mo^{5+} and Mo^{6+} species, respectively [67,68].

A catalyst with a higher sulfidation degree (MoS_2) would suggest that there was a lower metal–support interaction with the active metal, bringing about easier catalyst reduction and sulfidation [67]. The slight shift toward the lower BE of Mo 3d in the RhMo/ɣ-Al_2O_3 catalyst (Table S1) could be attributed to a weaker metal–support interaction (caused by electron effects of the defects at the surface on the alumina support), which enhances the HDS catalytic activity [68,69].

2.7. Transmission Electron Microscopy (TEM)

Information on active MoS_2 crystallite dispersion and sizes in the sulfided RhMo/ɣ-Al_2O_3 and RhMo-x/ɣ-Al_2O_3 (where x = AA, EDTA, CA) was obtained by means of TEM measurement. Figure 6a–d shows the distribution of MoS_2 crystallites in the sulfided catalysts with and without the chelating agents, and their statistical distribution results for the length of the MoS_2 slab. The addition of the chelating agents influenced the particle size distribution. The RhMo-CA/ɣ-Al_2O_3 had the lowest average diameter (1.86 nm) and the RhMo/ɣ-Al_2O_3 resulted in the highest average diameter (4.72 nm). The decrease of the MoS_2 slabs due to the chelating ligand's decomposition improved the dispersion of the active phase [70,71]. The average slab length in diameter observed for the catalysts are shown in Table 4, and the average slab length of the MoS_2 slab with the highest frequency was distributed between 2.5–6.0 nm. Along with these crystallites, there were a few regions with big agglomerations of molybdenum sulfide, as confirmed by the strings of highly stacked crystallites.

Table 4. Average length of MoS_2 crystallites in RhMo/Al_2O_3 and RhMo-x/ɣ-Al_2O_3 (x = EDTA, AA, CA).

Catalysts	Average Diameter $\pm$ SD (nm)
RhMo/ɣ-Al_2O_3	4.4 ($\pm$1.38)
RhMo-EDTA/ɣ-Al_2O_3	4.1 ($\pm$1.220)
RhMo-AA/ɣ-Al_2O_3	3.3 ($\pm$0.757)
RhMo-CA/ɣ-Al_2O_3	1.6 ($\pm$0.860)

The results for the MoS_2 slab average diameter in Table 4 indicated that the MoS_2 dispersion obtained for the RhMo catalysts decreased in the order of RhMo-CA/ɣ-Al_2O_3 > RhMo-AA/ɣ-Al_2O_3 > RhMo/ɣ-Al_2O_3 > RhMo-EDTA/ɣ-Al_2O_3. The higher dispersion for the chelated catalysts was due to the complexation of metal-chelating ligand, reducing the metal–support interaction and leading to the delay of the sulfidation of the metals. The high MoS_2 dispersion could facilitate the generation of more active sites [72–74].
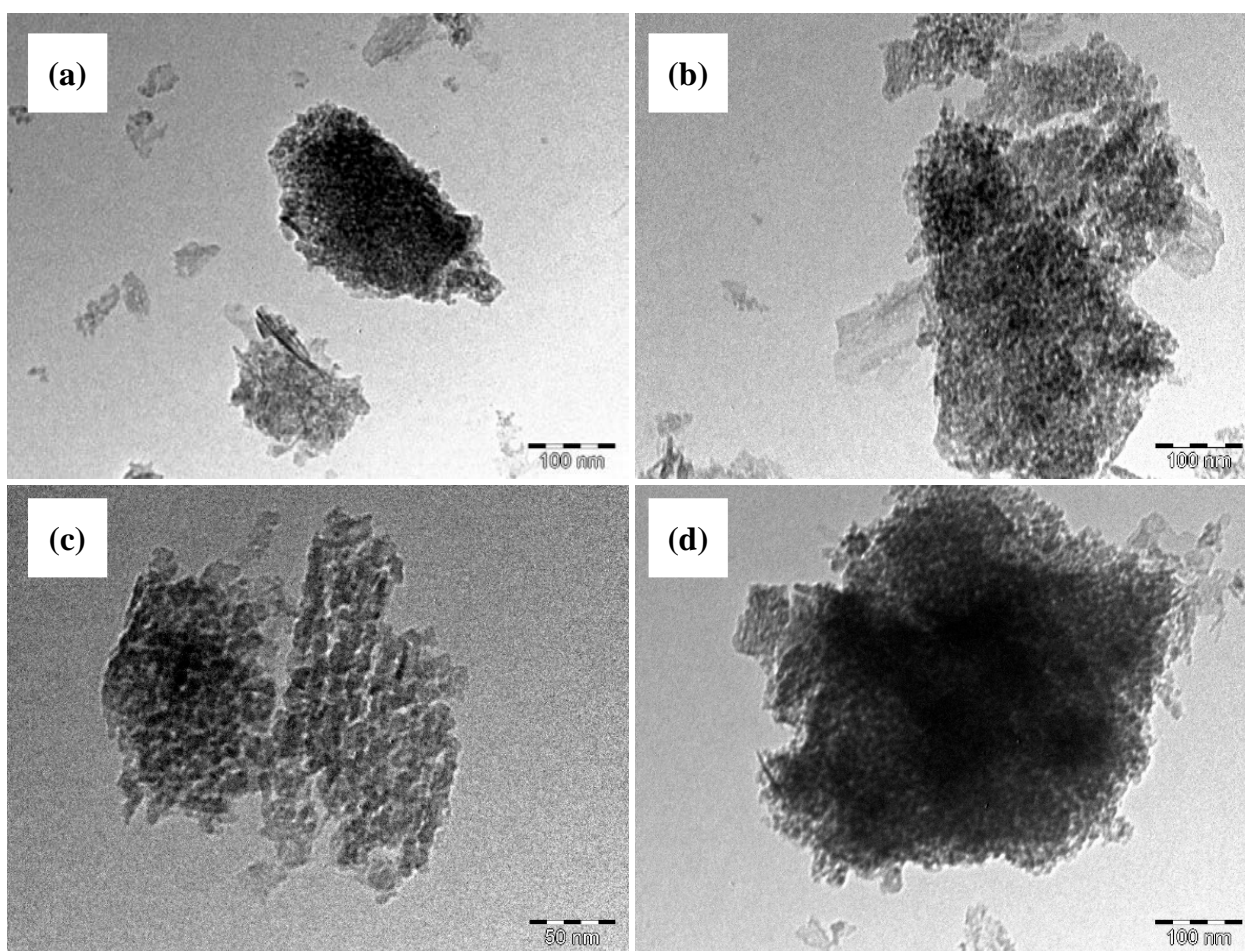
Figure 6. TEM images for (**a**) RhMo/ɣ-Al$_2$O$_3$, (**b**) RhMo-EDTA/ɣ-Al$_2$O$_3$, (**c**) RhMo-AA/ɣ-Al$_2$O$_3$, (**d**) RhMo-CA/ɣ-Al$_2$O$_3$.

2.8. Scanning Electron Microscopy (SEM)

The SEM images of RhMoO$_x$ are shown in Figure 7a,c,e,g for RhMo/ɣ-Al$_2$O$_3$ and RhMo-x/ɣ-Al$_2$O$_3$ (x = EDTA, AA, CA). The images showed that particles are closely spherical in shape with an average uniform distribution. All the samples had an average particle size (82.5–102.6 µm). Figure 7b,d,f,h represents the sulfided RhMo/ɣ-Al$_2$O$_3$ and RhMo-x/ɣ-Al$_2$O$_3$ (x = EDTA, AA, CA) catalysts, and the zoomed images show that all the chelated catalysts highly agglomerated with spherical-like materials with fluffy-like particles, which could indicate that the catalysts are porous in nature. The particle distributions for the sulfided catalysts could not be measured due to the high agglomeration of the particles.

2.9. Stability of Catalysts—TGA and DSC Thermal Analyses

TGA-DSC is a technique used for thermal analysis to characterize materials by measuring their change in mass as a function of temperature. It is coupled with DSC to provide complementary information such as measuring the heat flow as a function of time and temperature at a controlled environment.

RhMo/ɣ-Al$_2$O$_3$: The first weight loss (2.5%) for RhMo/ɣ-Al$_2$O$_3$ occurred in the range of 50–150 °C due to the desorption of the physically adsorbed water from the surface of the catalyst, and this was accompanied by a broad exothermic peak in the range of 120–210 °C (Figure 8a). A second weight loss of 3% was observed between 200–580 °C, and it was reflected by a very weak endothermic peak between 360–610 °C, associated with the decomposition of nitrate radical, hexaammonium molybdate and dihydroxylation [75].

An endothermic peak at 810 °C was observed, and it was attributed to the formation of a stable MoO_3 phase.
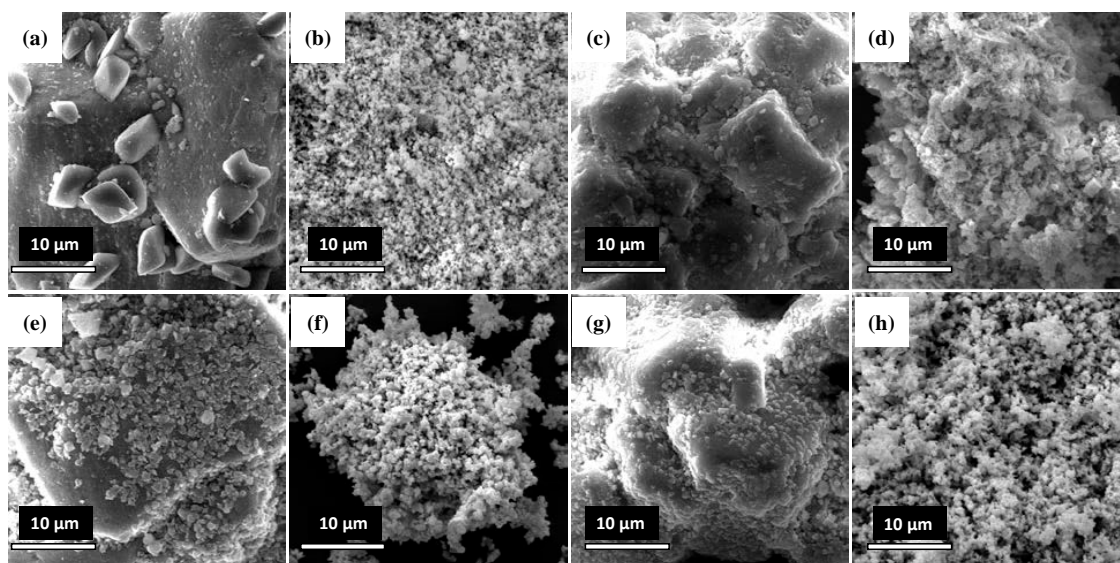
Figure 7. SEM images for RhMo/ɣ-Al$_2$O$_3$ (**a**) oxide, (**b**) sulfided; RhMo-EDTA/ɣ-Al$_2$O$_3$ (**c**) oxide, (**d**) sulfided; RhMo-AA/ ɣ-Al$_2$O$_3$ (**e**) oxide, (**f**) sulfided; RhMo-CA/ɣ-Al$_2$O$_3$ (**g**) oxide, (**h**) sulfided catalysts.
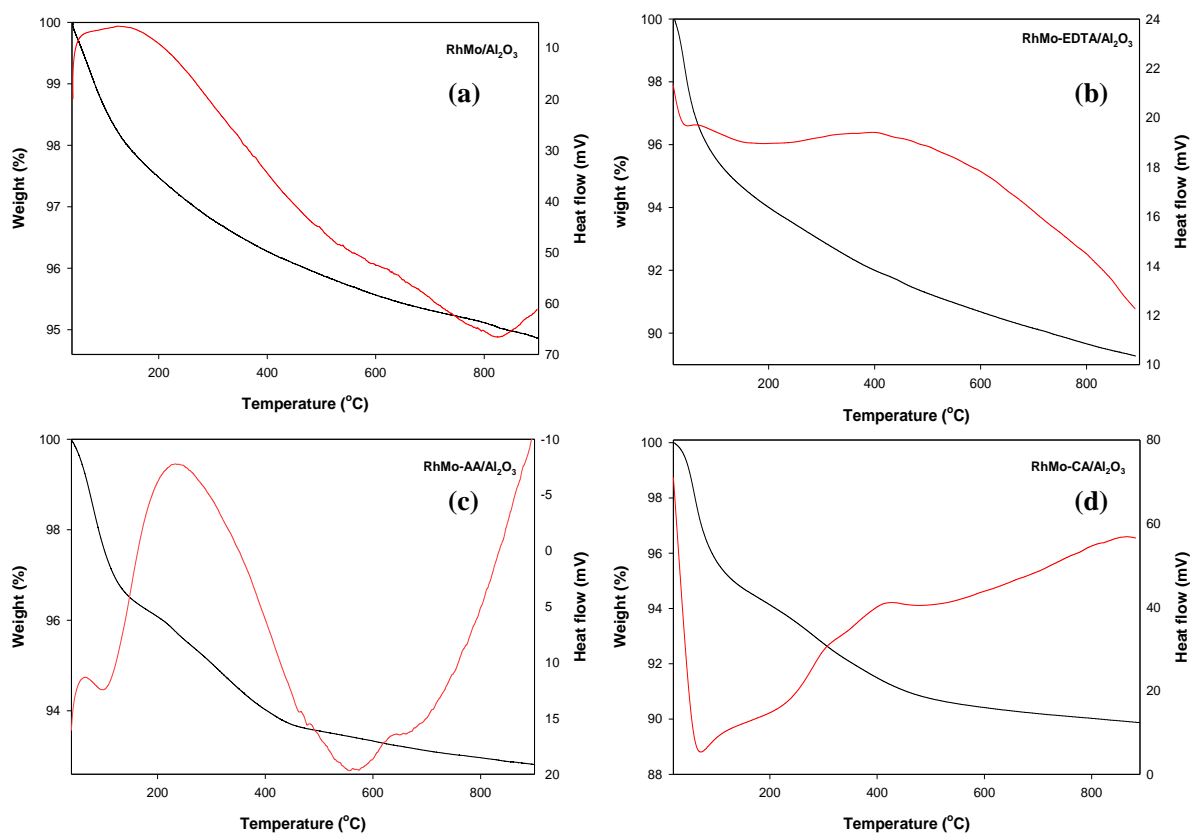
Figure 8. TGA-DSC curves of (**a**) RhMo/ɣ-Al$_2$O$_3$, (**b**) RhMo-EDTA/ɣ-Al$_2$O$_3$, (**c**) RhMo-AA/ɣ-Al$_2$O$_3$, (**d**) RhMo-CA/ ɣ-Al$_2$O$_3$ catalysts.

RhMo-EDTA/ɣ-Al$_2$O$_3$: The first weight loss (5.2%) in Figure 8b was below 100 °C and was mainly due to water desorption. From 160–800 °C, there was a gradual weight loss of

3% and not many events were happening in those stages. This weight loss was associated with the loss of the complex, and a partial dehydration–decomposition of the Rh and Mo species of RhMo-EDTA/ɣ-Al$_2$O$_3$. The first and second weight losses were accompanied by a broad exothermic peak at a maximum of 180 °C, corresponding to the decomposition of the complex. A broad exothermic peak between 280–670 °C was observed, and was due to the decomposition of EDTA and the further combustion of the residual organic matrix [76], and to the total transformation of the partially decomposed Rh and Mo precursor species into the catalyst oxidic precursor [77].

RhMo-AA/ɣ-Al$_2$O$_3$: The results obtained for RhMo-AA/ɣ-Al$_2$O$_3$ (Figure 8c) showed a weight loss (3.6%) taking place in the range of 50–150 °C followed by an exothermic peak 90 °C, which was mainly due to water desorption. The subsequent weight loss of 2.8% between 180–410 °C was attributed to the dehydration–decomposition of precursor species and the partial dehydroxylation of alumina [77]. A second exothermic peak occurred at a maximum of 280 °C, which corresponded to the decomposition of the complex (metal–AA) and the total decomposition and partial dehydration–decomposition of Rh and Mo precursor species. A third weight loss (1.8%) between 410–850 °C was due to the formation of the monometallic oxidic precursor. The DCS curve displayed an endothermic peak at a maximum of 580 °C.

RhMo-CA/ɣ-Al$_2$O$_3$: The results obtained for RhMo-CA/Al$_2$O$_3$ (Figure 8d) showed a weight loss of 5.2% below 150 °C, followed by an endothermic peak of 80 °C, was mainly due to H$_2$O removal. The second weight loss of 2.8% between 180–400 °C was attributed to a decomposition and combustion of the precursor species, and the complete breakdown of citric acid [46]. A broad and weak exothermic peak occurred at a maximum of 400 °C, which corresponded to the decomposition of the remaining complex (metal–CA) and the total decomposition and partial dehydration–decomposition of Rh and Mo precursor species. Above 400 °C, not much loss of weight loss was observed, and this indicated the formation of stable metallic oxidic precursors.

2.10. Catalytic Activity

The conversion of dibenzothiophene (DBT) was used to estimate the catalytic activity in HDS (Equation (1)). RhMo/ɣ-Al$_2$O$_3$ (88%) had the highest catalytic activity, and the activity for the chelated catalysts followed this order: RhMo-AA/ɣ-Al$_2$O$_3$ (73%) > RhMo-CA/ɣ-Al$_2$O$_3$ (72%) > RhMo-EDTA/ɣ-Al$_2$O$_3$ (68%) (Table 5). The observed catalytic results were ascribed to the introduction of the different ligands, which increased the metal–support interaction and increased the e-charge transfer (energy band gap) from the valance band Rh 4d orbital to the conduction band of the Mo species. The absence led to a weaker Mo-S bond strength, a higher concentration of CUS and a higher HDS activity [60]. Crystallite sizes were also observed to influence the catalytic activity, as RhMo/ɣ-Al$_2$O$_3$ (with crystallite size of 5.903 nm) presented the highest activity, and this may be due to the formation of bigger MoS$_2$ crystals when compared to others. A combined electron donating effect of the chelates, and the crystallite sizes of MoS$_2$, may have influenced the chelated catalyst activity.

Table 5. Catalytic performances of RhMo/ɣ-Al$_2$O$_3$ and RhMo-x/ɣ-Al$_2$O$_3$ (x = EDTA, AA, CA) in hydrotreating of DBT as simulated fuel.

Catalysts	Crystallite Sizes (nm)	E$_g$ Values	HDS (%)	BP(%)	PhCh(%)	HYD/DDS Ratio	TOF (h^{-1}) [a]
RhMo/ɣ-Al$_2$O$_3$	5.903	3.779	88	65	13	0.20	51
RhMo-EDTA/ɣ-Al$_2$O$_3$	5.770	4.394	68	16	1	0.06	60
RhMo-AA/ɣ-Al$_2$O$_3$	5.750	4.341	73	65	3	0.05	79
RhMo-CA/ɣ-Al$_2$O$_3$	5.809	4.478	72	36	2	0.06	223

Catalyst (molybdenum content) employed = 0.1 g (4.119 × 10^{-5} moles). Hydrodesulfurization (HDS) time = 6 h; reaction temperature = 300 °C; reaction pressure = 40 bar. Phenylcyclohexane (PhCh) or biphenyl (BP) [a] TOF, h^{-1}: (turnover frequency).

The chelated RhMo/ɣ-Al$_2$O$_3$ catalysts resulted in slightly lower catalytic activity due to the formation of rhodium-chelating ligands and a molybdenum–chelate complex. For all the catalysts, DBT converted mainly via the DDS pathway (Table 5). There was not much difference obtained in terms of selectivity when comparing the HYD/DDS selectivity ratio. RhMo/ɣ-Al$_2$O$_3$ showed a slightly higher HYD/DDS ratio of ~0.20 when compared to the chelated catalysts (see GC chromatogram, Figures S5–S7). The addition of the chelating ligands showed a slight difference, and therefore we can conclude that the addition of the chelating ligand on the catalysts did not have much influence on the selectivity (Table 5).

The HDS selectivity correlated linearly with the slab length of the MoS$_2$ phase (TEM), the longer slab length indicated a high ratio of edge/corner and better HDS selectivity, with RhMo/ɣ-Al$_2$O$_3$ presenting the longest slab length [64,77], and the edge sites only catalysed the HDS reaction [78]. The values presented by the current RhMo catalysts (Table 6) exhibit certain benefits and compare well with the other catalysts reported in the literature [79–84]. We concluded that the HDS % conversion and desulfurization route was influenced by the catalyst composition, the electronic properties and the HDS reaction conditions.

Table 6. Comparison of catalyst performance with literature reports in DBT hydrodesulfurization.

Catalysts	Model Compound	Reaction Temperature (°C)	HDS (%)	Reaction Pressure (Bar)	Reference
RhMo/ɣ-Al$_2$O$_3$	DBT	300	88	40	This work
RhMo-EDTA/ɣ-Al$_2$O$_3$	DBT	300	68	40	This work
RhMo-AA/ɣ-Al$_2$O$_3$	DBT	300	73	40	This work
RhMo-CA/ɣ-Al$_2$O$_3$	DBT	300	72	40	This work
Ni$_2$P	DBT	340	35	40	[79]
Ni$_2$P	TH-DBT	340	50	40	[79]
NiMoP/γ-Al$_2$O$_3$	DBT	<320	22–90	<25	[80]
Ru$_x$MoNi	DBT	320	24–92	54.5	[81]
NiMo	DBT	320	62	54.5	[81]
NiMo/TiO$_2$-6	DBT	300	90	20	[82]
NiMo/MCM-41-Na	DBT	300	>95	50	[83]
Fe-Zn/TiO$_2$-Al$_2$O$_3$	DBT	380	>98	40	[84]
RhMo/ɣ-Al$_2$O$_3$	DBT	310	84	50	[28]

Dibenzothiophene (DBT); TH-DBT = 1,2,3,4-tetrahydro-dibenzothiophene (TH-DBT).

2.11. Proposed Mechanism

The large energy gap (E$_g$) values of the chelated ligands RhMo-AA/ɣ-Al$_2$O$_3$ (4.341 eV), RhMo-EDTA/ɣ-Al$_2$O$_3$ (4.394 eV) and RhMo-CA/ɣ-Al$_2$O$_3$ (4.478 eV), supported the increased charge transfer of Rh, chelates and Mo species catalysts when compared to RhMo/ɣ-Al$_2$O$_3$ (3.779 eV). However, according to Figure 5a–d, the higher amount of Mo-S/RhMo-S phases are formed in the absence of a chelating ligand, owing to the electron transfer between the Rh and Mo-phase. Furthermore, the BE of O 1s increases upon chelation, confirming less neutralization of the surface O-H in ɣ-Al$_2$O$_3$ (O 1s 531.08 eV). The O 1s of RhMo/Al$_2$O$_3$ is 529.139 eV, and for RhMo-EDTA/Al$_2$O$_3$ is 529.280 eV (Figure 9).

Thus, this implies that ligand presence decreases the neutralization of the surface Brønsted acid site OH$^{\delta+}$ of ɣ-Al$_2$O$_3$ (an observed increase in the oxygen binding energies), and this prevents the formation of Mo-S/RhMo-S bonds, but more Rh-S bonds are formed due to the higher charge transfer between Rh and the chelating ligands (see Figure 5c,d). Generally, the free electrons promoted catalytic activities by donating electrons to the conduction band of the Mo species, thus promoting Mo-S/RhMo-S bond cleavage to form more coordinatively unsaturated sites (CUS) (Scheme 1). In a typical HDS reaction, the Rh$_2$O$_3$ phase is reduced to metallic rhodium (BE of Rh 3d$_{5/2}$ at 307.0–307.1 eV, predominately observed in RhMo/ɣ-Al$_2$O$_3$ [55]) and Rh$_2$O$_3$-x(RhO), with unpaired free electrons in the Rh 4d orbital and oxygen vacancies transferred to the conduction band of Mo species, thereby promoting the cleavage of Mo-S/RhMo-S to form the CUS. The increased charge transfer (energy gap (E$_g$) values) in chelated RhMo/ɣ-Al$_2$O$_3$ between Rh and Mo species

led to the excessive weakening of the Mo-S bond, preventing S-compound absorption on the active sites, thereby leading to reduced activity [84].
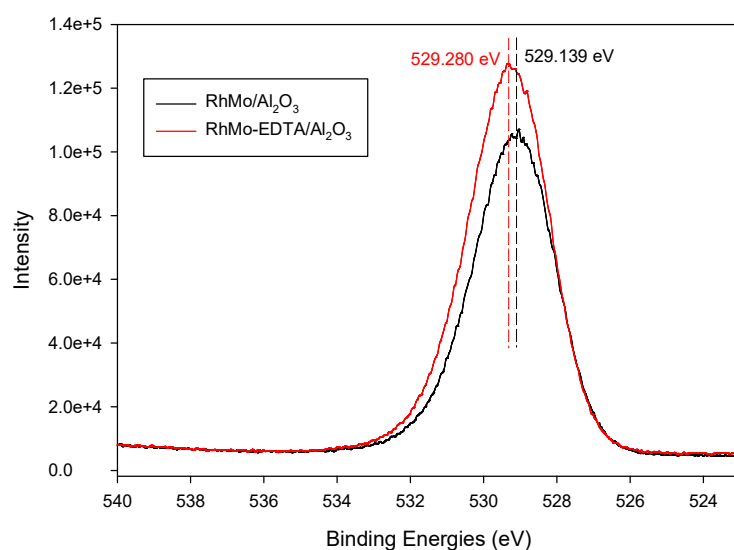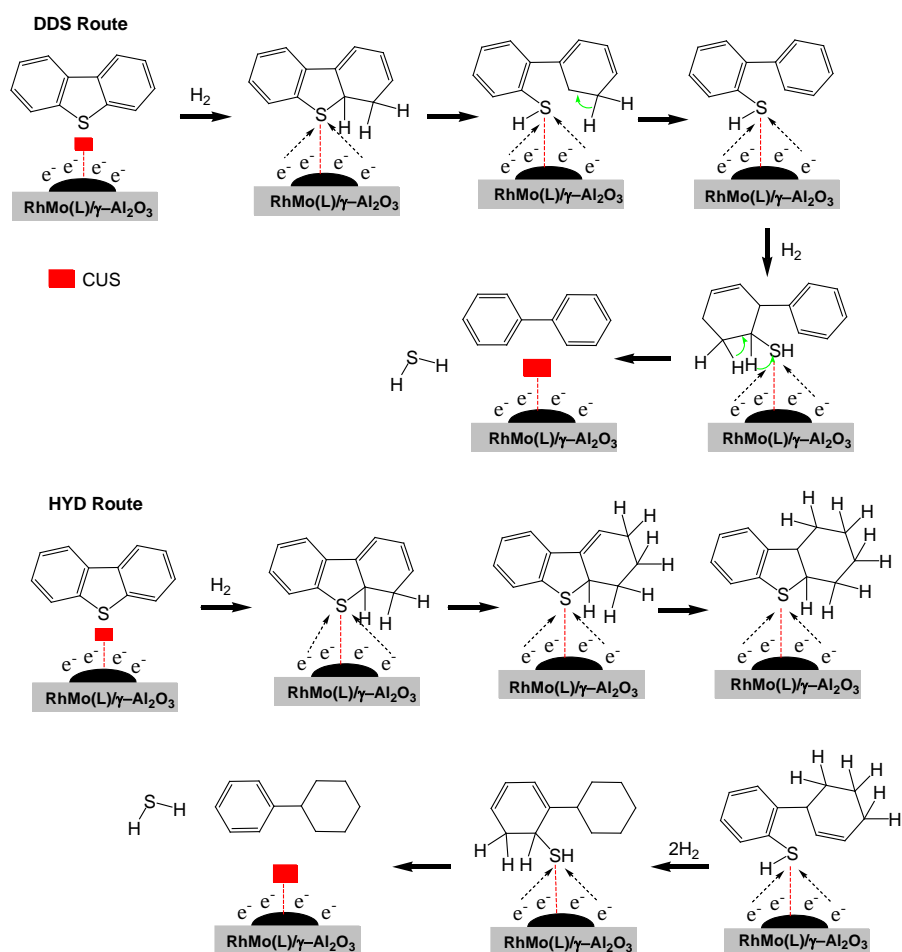

Figure 9. XPS spectra of O 1s of RhMo/ɣ-Al$_2$O$_3$ and RhMo-EDTA/ɣ-Al$_2$O$_3$.

Scheme 1. Proposed mechanisms of DDS and HDS reaction on RhMo chelated catalysts in HDS of DBT.

3. Experimental Section

3.1. Materials

All chemicals used were obtained from Merck/Sigma-Aldrich, South Africa. These include rhodium(III) chloride (98%), ammonium heptamolybdate (99%), ethylenediaminetetraacetic acid (EDTA, 97%), citric acid monohydrate (CA, 99.5%), acetic acid (AA, 99%), heptane, dibenzothiophene (98%) and gamma alumina support (γ-Al_2O_3).

3.2. Synthesis of RhMo Catalysts Prepared with Ethylenediaminetetraacetic Acid (EDTA), Citric Acid (CA) and Acetic Acid (AA)

Rh(x)Mo(y) catalysts were prepared by wet impregnations of the precursor salts [28]. *Unchelated catalyst*: Rh from $RhCl_3$ (0.0421 g, 2×10^{-4} mol) and Mo from $(NH_4)_6Mo_7O_{24} \cdot 4H_2O$ (0.496 g, 4×10^{-4} mol) were added in 30 mL deionized water to obtain the desired metal content ratio (Rh/Rh + Mo) 0.3, and the pH adjusted to pH = 9. The solution was added to γ-alumina (1 g), and the resulting mixture was transferred to a 100 mL Teflon-lined stainless steel autoclave, and hydrothermally treated at 453 K for 4 h. The resulting solid was filtered, dried at 393 K for 12 h and calcined at 773 K for 4 h to obtain the RhMo oxide on γ-alumina.

Chelated catalysts: Generally, for the synthesis of chelated catalyst, molar ratios 1:2 Rh to chelates (EDTA, CA and AA) was employed. RhMo-AA/γ-Al_2O_3: A mixture of $RhCl_3$ (0.0421 g, 2×10^{-4} mol), $(NH_4)_6Mo_7O_{24} \cdot 4H_2O$ (0.496 g, 4×10^{-4} mol) and AA (0.0241 g, 4×10^{-4} mol) was dissolved in 20 mL H_2O solution. RhMo-CA/γ-Al_2O_3: A mixture of $RhCl_3$ (0.0421 g, 2×10^{-4} mol), $(NH_4)_6Mo_7O_{24} \cdot 4H_2O$ (0.496 g, 4×10^{-4} mol) and AA (0.0770 g, 4×10^{-4} mol) was dissolved in 20 mL H_2O solution. RhMo-EDTA/γ-Al_2O_3: A mixture of $RhCl_3$ (0.0421 g, 2×10^{-4} mol), $(NH_4)_6Mo_7O_{24} \cdot 4H_2O$ (0.496 g, 4×10^{-4} mol) and EDTA (0.0745 g, 2×10^{-4} mol) was dissolved in 20 mL H_2O solution. In all of the solution mixtures, the molar ratio with Rh/Rh + Mo molar ratio of 0.3 was added to γ-Al_2O_3 (1 g, calcined at 500 °C) and the mixture was stirred for 4 h and pH adjusted to 9. The resulting solid was dried at 120 °C overnight to obtain RhMo-AA/γ-Al_2O_3, RhMo-CA/γ-Al_2O_3 and RhMo-EDTA/γ-Al_2O_3. For the chelated catalysts, RhMo-AA/γ-Al_2O_3, RhMo-CA/γ-Al_2O_3 and RhMo-EDTA/γ-Al_2O_3 were only treated at 120 °C to preserve chelating ligands (CA, AA and EDTA) in catalyst until the activation stage [46,50].

3.3. Catalyst Characterization

Ultraviolet-visible diffuse reflectance spectroscopy (DRS) and band gap energies of the catalysts were processed from a Shimadzu UV-vis DRS spectrophotometer UV-3100 UV-vis spectrophotometer from a wavelength range from 200 to 800 nm.

FT-IR spectroscopy of the catalysts was acquired using a Bruker Tensor 27 platinum ATR-FTIR spectrometer (wavelength range from 4000 to 400 cm^{-1}).

Thermogravimetric analysis (TGA-DSC) was measured using a Perkin Elmer STA 6000 at a heating range of 55 to 900 °C at 20 °C/min with N_2 flow of 30 mL min^{-1}.

X-ray powder diffraction (XRD) analysis was carried out on a Bruker D2 powder X-ray diffractometer using Cu radiation with a LynxEye detector with a scan range of 5 to 80° 2 theta.

Milled samples (RhMo/γ-Al_2O_3, RhMo-AA/γ-Al_2O_3, RhMo-CA/γ-Al_2O_3 and RhMo-EDTA/γ-Al_2O_3) were gold coated and imaged for morphological evaluation using a JOEL 7001f scanning electron microscope (SEM). JEOL JEM-2010 transmission electron microscope (TEM) operated at 200 kV was employed for TEM imaging.

X-ray photoelectron spectrometer (XPS) was performed on a Kratos Axis Ultra X-ray photoelectron spectrometer equipped with a monochromatic Al K_α source (1486.6 eV).

3.4. Catalyst Sulfidation and Hydrodesulfurization Measurements

The sulfidation and HDS tests were carried in a 2 L Parr pressure reactor 4842 (350 bar, max tem = 425 °C). For catalyst sulfidation: HDS catalysts (2 g, mol/mL ratio of Mo:DBT (~1:100)) were pressurized to 4.0 MPa (40 bar) in a 100 mL heptane solution containing

10 wt.% of CS_2 (sulfiding agent) under hydrogen flow (40 mL/min) for 4 h and at 573 K to ensure complete sulfidation.

After sulfidation, the reactor was cooled down to room temperature for the dibenzothiophene HDS test. At this temperature, the liquid feed was switched to dibenzothiophene solution (0.22 g, 1.194×10^{-5} mol/mL). The temperature was adjusted to 573 K under H_2 pressure of 4.0 MPa (40 bar) and maintained for 6 h. The dibenzothiophene content was measured with an Agilent 6890 gas chromatograph equipped with a FID detector and a 30 m × 0.25 mm × 0.25 μm capillary column (ZB-5MSi, 5% Phenyl column). HDS catalytic activity was estimated using (3):

$$X_{HDS}(\%) = \frac{C^0_{DBT} - C_{DBT}}{C^0_{DBT}} \times 100 \tag{3}$$

where C^0_{DBT} is the DBT content in the feedstock (wt.%) and C_{DBT} is the DBT content in the products (wt.%) [29]. Therefore, the catalytic selectivity ratio between the hydrogenation (HYD) and direct desulfurization (DDS) is estimated from Equation (4):

$$S_{HYD}/S_{DDS} = \frac{C_x}{C^0_{DBT} - C_{DBT}} \tag{4}$$

where C_x is the content of phenylcyclohexane (PhCh) or biphenyl (BP) [30].

4. Conclusions

In the present work, a series of new catalysts (RhMo/Al_2O_3, RhMo-x/Al_2O_3 (where x = EDTA, AA, CA) were successfully synthesized and characterized. The UV-vis analysis confirmed the presence of octahedral molybdate species between 320–360 nm for RhMo/Al_2O_3, and the shift to a lower wavelength in the visible part of 220 nm for the chelated catalysts was observed and indicated the formation of less polymerized molybdate species and heteropoplymolybdates. Band gaps of 3.779 eV (RhMo/ɣ-Al_2O_3), 4.341 eV (RhM-EDTA/ɣ-Al_2O_3), 4.394 eV (RhMo-AA/ɣ-Al_2O_3) and 4.478 eV (RhMo-CA/ɣ-Al_2O_3) were obtained. The TEM imaging confirmed that the materials had fringe-like morphologies, deemed as MoS_2 slabs. The chelated catalysts showed a greater dispersion when compared with the unchelated catalysts, and this was confirmed by XRD analysis by the absence of crystalline peaks for the chelated catalysts. RhMo/Al_2O_3 resulted in higher catalytic activity when compared with the chelated catalysts, and this was confirmed by XPS showing more MoS_2 phases of the RhMo/Al_2O_3 catalyst to be (63%), and it was also confirmed by HDS activity where RhMo/Al_2O_3 exhibited the highest DBT conversion of (88%). The addition of the chelating ligands (EDTA, AA and CA) resulted in lower HDS activity. Since this is a new catalyst, a lot of parameters must be investigated, such as the sulfidation temperature for Rh, the crystallite size effects, the molar ratio of Rh:chelating ligand to be used, and the type of the chelating ligand to be used. This would help to understand the catalyst and how the activity could be enhanced.

Supplementary Materials: The following are available online at https://www.mdpi.com/article/10.3390/catal11111398/s1, Figure S1: The E_g values for RhMo/Al_2O_3, RhMo-x/Al_2O_3 (x = EDTA, AA, CA) obtained from a UV-Vis spectra; Figure S2. FT-IR spectra of RhMo/ɣ-Al_2O_3, RhMo-EDTA/ɣ-Al_2O_3, RhMo-AA/ɣ-Al_2O_3, and RhMo-CA/ɣ-Al_2O_3 catalysts; Figure S3. EDX analysis for (**a**) RhMo/Al_2O_3, (**b**) RhMo-EDTA/Al_2O_3, (**c**) RhMo-AA/Al_2O_3, (**d**) RhMo-CA/Al_2O_3 catalysts.; Figure S4. XPS spectra for RhMo/Al_2O_3 different elemental contributions of (**a**) O 1s, (**b**) C 1s, (**c**) Al 2p, (**d**) Al 2s; Figure S5. XPS spectra for CoMo-EDTA/ɣ-Al_2O_3 different elemental contributions of (**a**) O 1s, (**b**) C 1s, (**c**) Al 2p, (**d**) Al 2s; Figure S6. GC chromatogram of DBT before HDS; Figure S7. GC chromatogram of DBT after HDS using (**A**) RhMo/Al_2O_3, (**B**) RhMo-EDTA/Al_2O_3, (**C**) RhMo-AA/Al_2O_3, (**D**) RhMo-CA/Al_2O_3, DBT = dibenzothiophene, BP = biphenyl, PhCH = biphenyl cyclohexane, BCH = bicyclohexyl, THDBT= tetrahydrodibenzothiophene; Table S1. XPS parameters of the different distributions (BE) of Mo 3d obtained for chelated and unchelated RhMo/Al_2O_3

catalysts; Table S2. XPS parameters of the contributions of Rh 3d obtained for unchelated and chelated RhMo/Al$_2$O$_3$ catalysts.

References

1. Dembaremba, T.O.; Ogunlaja, A.S.; Tshentu, Z.R. Coordination polymers and polymer nanofibers for effective adsorptive desulfurization. In *Nanocomposites Desulfurization Fuels*; Saleh, T., Ed.; IGI Global: Hershey, PA, USA, 2020; pp. 168–234. Available online: https://www.igi-global.com/chapter/coordination-polymers-and-polymer-nanofibers-for-effective-adsorptive-desulfurization/246161 (accessed on 4 March 2021). [CrossRef]
2. Tahira, S.; Qazib, U.Y.; Naseema, Z.; Tahira, N.; Zahida, M.; Javaidc, R.; Shahid, I. Deep eutectic solvents as alternative green solvents for the efficient desulfurization of liquid fuel: A comprehensive review. *Fuel* **2021**, *305*, 121502. [CrossRef]
3. Nascimento, I.G.; Locatel, W.R.; Magalhães, B.C.; Travalloni, L.; Zotin, J.L.; da Silva, M.A.P. Kinetics of dibenzothiophene hydrodesulfurization reactions using CoMoP/Al$_2$O$_3$ and NiMoP/Al$_2$O$_3$. *Catal. Today* **2021**, *381*, 200–208. [CrossRef]
4. Mundotiya, S.; Singh, R.; Saha, S.; Kakkar, R.; Pal, S.; Kunzru, D.; Pala, R.G.S.; Sivakumar, S. Effect of Sodium on Ni-Promoted MoS$_2$ Catalyst for Hydrodesulfurization Reaction: Combined Experimental and Simulation Study. *Energy Fuels* **2021**, *35*, 2368–2378. [CrossRef]
5. Huang, T.; Peng, Q.; Gai, H.; Fan, Y. Surfactant-Confined Synthesis of CoMoS Catalysts Using Polyoxometalate Precursors for Superior Fuel Hydrodesulfurization. *Energy Fuels* **2021**, *35*, 2402–2415. [CrossRef]
6. Zhang, M.; Wang, C.; Han, Z.; Wang, K.; Zhang, Z.; Guan, G.; Abudula, A.; Xu, G. Catalyst Ni-Mo/Al$_2$O$_3$ promoted with infrared heating calcination for hydrodesulfurization of shale oil. *Fuel* **2021**, *305*, 121537. [CrossRef]
7. Vinogradov, N.A.; Glotov, A.P.; Savinov, A.A.; Vutolkina, A.V.; Vinokurov, V.A.; Pimerzin, A.A. The mesoporous silicate-alumina composites application as supports for bifunctional sulfide catalysts for n-hexadecane hydroconversion. *J. Porous Mater.* **2021**, *28*, 1449–1458. [CrossRef]
8. Ghosh, S.; Courthéoux, L.; Brunet, S.; Lacroix-Desmazes, P.; Pradel, A.; Girard, E.; Uzio, D. Hybrid CoMoS—Polyaniline nanowires catalysts for hydrodesulfurisation applications. *Appl. Catal. A Gen.* **2021**, *623*, 118264. [CrossRef]
9. Soltanali, S.; Mashayekhi, M.; Mohaddecy, S.R.S. Comprehensive investigation of the effect of adding phosphorus and/or boron to NiMo/γ-Al$_2$O$_3$ catalyst in diesel fuel hydrotreating. *Process Saf. Environ. Prot.* **2020**, *137*, 273–281. [CrossRef]
10. Hamidi, R.; Khoshbin, R.; Karimzadeh, R. Facile fabrication, characterization and catalytic activity of a NiMo/Al$_2$O$_3$ nanocatalyst via a solution combustion method used in a low temperature hydrodesulfurization process: The effect of fuel to oxidant ratio. *RSC Adv.* **2020**, *10*, 12439–12450. [CrossRef]
11. Shafiq, I.; Shafique, S.; Akhter, P.; Yang, W.; Hussain, W. Recent developments in alumina supported hydrodesulfurization catalysts for the production of sulfur-free refinery products: A technical review. *Catal. Rev.* **2020**, 1–86. [CrossRef]
12. Vutolkina, A.V.; Glotov, A.P.; Zanina, A.V.; Mahmutov, D.F.; Maksimov, A.L.; Karakhanov, E.A. Mesoporous Al-HMS and Al-MCM-41 supported Ni-Mo sulfide catalysts for HYD and HDS via in situ hydrogen generation through a WGSR. *Catal. Today* **2019**, *329*, 156–166. [CrossRef]
13. Rinaldi, N.; Kubota, T.; Okamoto, Y. Effect of citric acid addition on the hydrodesulfurization activity of MoO$_3$/Al$_2$O$_3$ catalysts. *Appl. Catal. A: Gen.* **2010**, *374*, 228–236. [CrossRef]
14. Ninh, T.K.T.; Massin, L.; Laurenti, D.; Vrinat, M. A new approach in the evaluation of the support effect for NiMo hydrodesulfurization catalysts. *Appl. Catal. A: Gen.* **2011**, *407*, 29–39. [CrossRef]
15. Sun, M.; Nicosia, D.; Prins, R. The effects of fluorine, phosphate and chelating agents on hydrotreating catalysts and catalysis. *Catal. Today* **2003**, *86*, 173–189. [CrossRef]
16. Zhang, X.; Wei, W.; Yin, X.; Li, G.; Li, L.; Guo, R.; Liu, X.; Guo, Q.; Shen, B. Migration and rearrangement of Fe–Zn species in the preparation of Fe–Zn bimetallic catalysts and their effects on the hydrodesulfurization reactivity. *Energy Fuels* **2021**, *35*, 16768–16777. [CrossRef]
17. Ramírez, J.; Romualdo-Escobar, D.; Castillo-Villalón, P.; Gutiérrez-Alejandre, A. Improved NiMoSA catalysts: Analysis of EDTA post-treatment in the HDS of 4,6-DMDBT. *Catal. Today* **2020**, *349*, 168–177. [CrossRef]

18. Hussain, M.; Song, S.-K.; Lee, J.-H.; Ihm, S.-K. Characteristics of CoMo catalysts supported on modified MCM-41 and MCM-48 materials for thiophene hydrodesulfurization. *Ind. Eng. Chem. Res.* **2006**, *45*, 536–543. [CrossRef]

19. Hussain, M.; Ihm, S.K. Synthesis, characterization, and hydrodesulfurization activity of new mesoporous carbon supported transition metal sulfide catalysts. *Ind. Eng. Chem. Res.* **2009**, *48*, 698–707. [CrossRef]

20. Hussain, M.; Yun, J.S.; Ihm, S.-K.; Russo, N.; Geobaldo, F. Synthesis, characterization, and thiophene hydrodesulfurization activity of novel macroporous and mesomacroporous carbon. *Ind. Eng. Chem. Res.* **2011**, *50*, 2530–2535. [CrossRef]

21. Aray, Y.; Rodriguez, J.; Vega, D.; Rodriguez-Arias, E.N. Correlation of the topology of the electron density of pyrite-type transition metal sulfides with their catalytic activity in hydrodesulfurization. *Angew. Chem. Int. Ed.* **2000**, *39*, 3810–3813. [CrossRef]

22. Vissers, J.P.R.; Groot, C.K.; Van Oers, E.M.; Beer, D.; Prins, R. Carbon-supported transition metal sulfides. *Bull. Des Sociétés Chim. Belg.* **1984**, *93*, 813–822. [CrossRef]

23. Ledoux, M.J.; Michaux, O.; Agostini, G.; Panissod, P. The influence of sulfide structures on the hydrodesulfurization activity of carbon-supported catalysts. *J. Catal.* **1986**, *102*, 275–288. [CrossRef]

24. Raybaud, P.; Hafner, J.; Kresse, G.; Toulhoat, H. Ab initio density functional studies of transition-metal sulphides: II. Electronic structure. *J. Phys. Condens. Matter* **1997**, *9*, 11107. [CrossRef]

25. Toulhoat, H.; Raybaud, P.; Kasztelan, S.; Kresse, G.; Hafner, J. Transition metals to sulfur binding energies relationship to catalytic activities in HDS: Back to Sabatier with first principle calculations. *Catal. Today* **1999**, *50*, 629–636. [CrossRef]

26. Bataille, F.; Lemberton, J.L.; Michaud, P.; Pérot, G.; Vrinat, M.; Lemaire, M.; Kasztelan, S. Alkyldibenzothiophenes hydrodesulfurization-promoter effect, reactivity, and reaction mechanism. *J. Catal.* **2000**, *191*, 409–422. [CrossRef]

27. Lee, J.; Ishihara, A.; Dumeignil, F.; Miyazaki, K.; Oomori, Y.; Qian, E.W.; Kabe, T. Novel hydrodesulfurization catalysts derived from a rhodium carbonyl complex. *J. Mol. Catal. A Chem.* **2004**, *209*, 155–162. [CrossRef]

28. Giraldo, S.A.; Pinzón, M.H.; Centeno, A. Behavior of catalysts with rhodium in simultaneous hydrodesulfurization and hydrogenation reactions. *Catal. Today* **2008**, *133*, 239–243. [CrossRef]

29. Rana, M.S.; Ramírez, J.; Gutiérrez-Alejandre, A.; Ancheyta, J.; Cedeño, L.; Maity, S.K. Support effects in CoMo hydrodesulfurization catalysts prepared with EDTA as a chelating agent. *J. Catal.* **2007**, *246*, 100–108. [CrossRef]

30. Stanislaus, A.; Marafi, A.; Rana, M.S. Recent advances in the science and technology of ultra-low sulfur diesel (ULSD) production. *Catal. Today* **2010**, *153*, 1–68. [CrossRef]

31. Ríos-Caloch, G.; Santes, V.; Escobar, J.; Valle-Orta, M.; Barrera, M.C.; Hernández-Barrera, M. Effect of chitosan addition on NiMo/Al$_2$O$_3$ catalysts for Dibenzothiophene Hydrodesulfurization. *Int. J. Chem. Reactor Eng.* **2012**, *10*, 1–24. [CrossRef]

32. Bui, N.Q.; Geantet, C.; Berhault, G. Activation of regenerated CoMo/Al$_2$O$_3$ hydrotreating catalysts by organic additives–The particular case of maleic acid. *Appl. Catal. A Gen.* **2019**, *572*, 185–196. [CrossRef]

33. Mendes, F.M.; Schmal, M. The cyclohexanol dehydrogenation on Rh-CuAl$_2$O$_3$ catalysts Part 1. Characterization of the catalyst. *Appl. Catal. A Gen.* **1997**, *151*, 393–408. [CrossRef]

34. Bergwerff, J.A.; Visser, T.; Weckhuysen, B.M. On the interaction between Co-and Mo-complexes in impregnation solutions used for the preparation of Al$_2$O$_3$-supported HDS catalysts: A combined Raman/UV–vis–NIR spectroscopy study. *Catal. Today* **2008**, *130*, 117–125. [CrossRef]

35. Vatutina, Y.V.; Klimov, O.V.; Stolyarova, E.A.; Nadeina, K.A.; Danilova, I.G.; Chesalov, Y.A.; Noskov, A.S. Influence of the phosphorus addition ways on properties of CoMo-catalysts of hydrotreating. *Catal. Today* **2019**, *329*, 13–23. [CrossRef]

36. Matralis, H.; Papadopoulou, C.; Lycourghiotis, A. Fluorinated hydrotreatment catalysts effect of the deposition order of F− ions on F-CoMo/γ-Al$_2$O$_3$ catalysts. *Appl. Catal. A Gen.* **1994**, *116*, 221–236. [CrossRef]

37. Papadopoulou, C.; Vakros, J.; Matralis, H.K.; Voyiatzis, G.A.; Kordulis, C. Preparation, characterization, and catalytic activity of CoMo/γ-Al$_2$O$_3$ catalysts prepared by equilibrium deposition filtration and conventional impregnation techniques. *J. Colloid Interface Sci.* **2004**, *274*, 159–166. [CrossRef]

38. Huirache-Acuña, R.; Zepeda, T.A.; Rivera-Muñoz, E.M.; Nava, R.; Loricera, C.V.; Pawelec, B. Characterization and HDS performance of sulfided CoMoW catalysts supported on mesoporous Al-SBA-16 substrates. *Fuel* **2015**, *149*, 149–161. [CrossRef]

39. Rinaldi, N.; Al-Dalama, K.; Kubota, T.; Okamoto, Y. Preparation of Co–Mo/B$_2$O$_3$/Al$_2$O$_3$ catalysts for hydrodesulfurization: Effect of citric acid addition. *Appl. Catal. A Gen.* **2009**, *360*, 130–136. [CrossRef]

40. Zhang, Y.; Han, W.; Long, X.; Nie, H. Redispersion effects of citric acid on CoMo/γ-Al$_2$O$_3$ hydrodesulfurization catalysts. *Catal. Commun.* **2016**, *82*, 20–23. [CrossRef]

41. Weber, R. Effect of local structure on the UV-Visible absorption edges of molybdenum oxide clusters and supported molybdenum oxides. *J. Catal.* **1995**, *151*, 470–474. [CrossRef]

42. Tian, H.; Roberts, C.A.; Wachs, I.E. Molecular structural determination of molybdena in different environments: Aqueous solutions, bulk mixed oxides, and supported MoO$_3$ catalysts. *J. Phys. Chem. C* **2010**, *114*, 14110–14120. [CrossRef]

43. Xu, J.; Huang, T.; Fan, Y. Highly efficient NiMo/SiO$_2$-Al$_2$O$_3$ hydrodesulfurization catalyst prepared from gemini surfactant-dispersed Mo precursor. *Appl. Catal. B Environ.* **2017**, *203*, 839–850. [CrossRef]

44. Escobar, J.; Barrera, M.C.; Gutiérrez, A.W.; Terrazas, J.E. Benzothiophene hydrodesulfurization over NiMo/alumina catalysts modified by citric acid. Effect of addition stage of organic modifier. *Fuel Process. Technol.* **2017**, *156*, 33–42. [CrossRef]

45. Cabello, C.I.; Cabrerizo, F.M.; Alvarez, A.; Thomas, H.J. Decamolybdodicobaltate (III) heteropolyanion: Structural, spectroscopical, thermal and hydrotreating catalytic properties. *J. Mol. Catal. A Chem.* **2002**, *186*, 89–100. [CrossRef]

46. Valencia, D.; Klimova, T. Citric acid loading for MoS$_2$-based catalysts supported on SBA-15. New catalytic materials with high hydrogenolysis ability in hydrodesulfurization. *Appl. Catal. B Environ.* **2013**, *129*, 137–145. [CrossRef]

47. Yurum, A.; Karakas, G. Synthesis of Na-, Fe-, and Co-promoted TiO$_2$/multiwalled carbon nanotube composites and their use as a photocatalyst. *Turk. J. Chem.* **2017**, *41*, 440–454. [CrossRef]

48. Trakarnpruk, W.; Seentrakoon, B. Hydrodesulfurization activity of MoS$_2$ and bimetallic catalysts prepared by in situ decomposition of thiosalt. *Ind. Eng. Chem. Res.* **2007**, *46*, 1874–1882. [CrossRef]

49. Alonso, G.; Petranovskii, V.; Del Valle, M.; Cruz-Reyes, J.; Licea-Claverie, A.; Fuentes, S. Preparation of WS$_2$ catalysts by in situ decomposition of tetraalkylammonium thiotungstates. *Appl. Catal. A Gen.* **2000**, *197*, 87–97. [CrossRef]

50. Badoga, S.; Mouli, K.C.; Soni, K.K.; Dalai, A.K.; Adjaye, J. Beneficial influence of EDTA on the structure and catalytic properties of sulfided NiMo/SBA-15 catalysts for hydrotreating of light gas oil. *Appl. Catal. B Environ.* **2012**, *125*, 67–84. [CrossRef]

51. Calderón-Magdaleno, M.Á.; Mendoza-Nieto, J.A.; Klimova, T.E. Effect of the amount of citric acid used in the preparation of NiMo/SBA-15 catalysts on their performance in HDS of dibenzothiophene-type compounds. *Catal. Today.* **2014**, *220*, 78–88. [CrossRef]

52. Chen, S.; Luo, L.; Cheng, X. Influence of preparation method on the performance of Pd/ZrO$_2$-Al$_2$O$_3$ catalysts for HDS. *Indian J. Chem. Technol.* **2009**, *16*, 272–277.

53. Gutiérrez, O.Y.; Pérez, F.; Fuentes, G.A.; Bokhimi, X.; Klimova, T. Deep HDS over NiMo/Zr-SBA-15 catalysts with varying MoO$_3$ loading. *Catal. Today* **2008**, *130*, 292–301. [CrossRef]

54. Hara, K.; Iwahashi, K.; Takakusagi, S.; Uosaki, K.; Sawamura, M. Construction of self-assembled monolayer terminated with N-heterocyclic carbene–rhodium(I) complex moiety. *Surf. Sci.* **2007**, *601*, 5127–5132. [CrossRef]

55. Larichev, Y.V.; Netskina, O.V.; Komova, O.V.; Simagina, V.I. Comparative XPS study of Rh/Al$_2$O$_3$ and Rh/TiO$_2$ as catalysts for NaBH$_4$ hydrolysis. *Int. J. Hydrog. Energy* **2010**, *35*, 6501–6507. [CrossRef]

56. Masud, J.; Van Nguyen, T.; Singh, N.; McFarland, E.; Ikenberry, M.; Hohn, K.; Hwang, B.J. A Rh$_x$S$_y$/C catalyst for the hydrogen oxidation and hydrogen evolution reactions in HBr. *J. Electrochem. Soc.* **2015**, *162*, F455. [CrossRef]

57. Galtayries, A.; Wisniewski, S.; Grimblot, J. Formation of thin oxide and sulphide films on polycrystalline molybdenum foils: Characterization by XPS and surface potential variations. *J. Electron Spectrosc. Relat. Phenom.* **1997**, *87*, 31–44. [CrossRef]

58. Venezia, A.M. X-ray photoelectron spectroscopy (XPS) for catalysts characterization. *Catal. Today* **2003**, *77*, 359–370. [CrossRef]

59. Budukva, S.V.; Klimov, O.V.; Uvarkina, D.D.; Chesalov, Y.A.; Prosvirin, I.P.; Larina, T.V.; Noskov, A.S. Effect of citric acid and triethylene glycol addition on the reactivation of CoMo/γ-Al2O3 hydrotreating catalysts. *Catal. Today* **2019**, *329*, 35–43. [CrossRef]

60. Xu, J.; Guo, Y.; Huang, T.; Fan, Y. Hexamethonium bromide-assisted synthesis of CoMo/graphene catalysts for selective hydrodesulfurization. *Appl. Catal. B Environ.* **2019**, *244*, 385–395. [CrossRef]

61. Huang, T.; Xu, J.; Fan, Y. Effects of concentration and microstructure of active phases on the selective hydrodesulfurization performance of sulfided CoMo/Al$_2$O$_3$ catalysts. *Appl. Catal. B Environ.* **2018**, *220*, 42–56. [CrossRef]

62. Matsumoto, K.; Matsumoto, T.; Kawano, M.; Ohnuki, H.; Shichi, Y.; Nishide, T.; Sato, T. Syntheses and crystal structures of disulfide-bridged binuclear ruthenium compounds: The First UV—Vis, Raman, ESR, and XPS Spectroscopic Characterization of a Valence-Averaged Mixed-Valent RuIIISSRuII Core. *J. Am. Chem. Soc.* **1996**, *118*, 3597–3609. [CrossRef]

63. Tang, M.; Zhou, L.; Du, M.; Lyu, Z.; Wen, X.D.; Li, X.; Ge, H. A novel reactive adsorption desulfurization Ni/MnO adsorbent and its hydrodesulfurization ability compared with Ni/ZnO. *Catal. Commun.* **2015**, *61*, 37–40. [CrossRef]

64. Liu, B.; Chai, Y.; Li, Y.; Wang, A.; Liu, Y.; Liu, C. Effect of sulfidation atmosphere on the performance of the CoMo/γ-Al$_2$O$_3$ catalysts in hydrodesulfurization of FCC gasoline. *Appl. Catal. A Gen.* **2014**, *471*, 70–79. [CrossRef]

65. Wang, H.; Liu, S.; Smith, K.J. Understanding selectivity changes during hydrodesulfurization of dibenzothiophene on Mo2C/carbon catalysts. *J. Catal.* **2019**, *369*, 427–439. [CrossRef]

66. Rashidi, F.; Sasaki, T.; Rashidi, A.M.; Kharat, A.N.; Jozani, K.J. Ultradeep hydrodesulfurization of diesel fuels using highly efficient nanoalumina-supported catalysts: Impact of support, phosphorus, and/or boron on the structure and catalytic activity. *J. Catal.* **2013**, *299*, 321–335. [CrossRef]

67. Wang, X.; Du, P.; Chi, K.; Duan, A.; Xu, C.; Zhao, Z.; Zhang, H. Synthesis of NiMo catalysts supported on mesoporous silica FDU-12 with different morphologies and their catalytic performance of DBT HDS. *Catal. Today* **2017**, *291*, 146–152. [CrossRef]

68. Nikulshina, M.; Kokliukhin, A.; Mozhaev, A.; Nikulshin, P. CoMo/Al$_2$O$_3$ hydrotreating catalysts prepared from single Co$_2$Mo$_{10}$-heteropolyacid at extremely high metal loading. *Catal. Commun.* **2019**, *127*, 51–57. [CrossRef]

69. Muhammad, Y.; Rahman, A.U.; Rashid, H.U.; Sahibzada, M.; Subhan, S.; Tong, Z. Hydrodesulfurization of dibenzothiophene using Pd-promoted Co–Mo/Al$_2$O$_3$ and Ni–Mo/Al$_2$O$_3$ catalysts coupled with ionic liquids at ambient operating conditions. *RSC Adv.* **2019**, *9*, 10371–10385. [CrossRef]

70. Pereyma, V.Y.; Klimov, O.V.; Prosvirin, I.P.; Gerasimov, E.Y.; Yashnik, S.A.; Noskov, A.S. Effect of thermal treatment on morphology and catalytic performance of NiW/Al$_2$O$_3$ catalysts prepared using citric acid as chelating agent. *Catal. Today* **2018**, *305*, 162–170. [CrossRef]

71. Zhang, M.H.; Fan, J.Y.; Chi, K.; Duan, A.J.; Zhao, Z.; Meng, X.L.; Zhang, H.L. Synthesis, characterization, and catalytic performance of NiMo catalysts supported on different crystal alumina materials in the hydrodesulfurization of diesel. *Fuel Process. Technol.* **2017**, *156*, 446–453. [CrossRef]

72. Shimizu, T.; Hiroshima, K.; Honma, T.; Mochizuki, T.; Yamada, M. Highly active hydrotreatment catalysts prepared with chelating agents. *Catal. Today* **1998**, *45*, 271–276. [CrossRef]

73. Okamoto, Y.; Ochiai, K.; Kawano, M.; Kubota, T. Evaluation of the maximum potential activity of Co–Mo/Al$_2$O$_3$ catalysts for hydrodesulfurization. *J. Catal.* **2004**, *222*, 143–151. [CrossRef]

74. Yoosuk, B.; Kim, J.H.; Song, C.; Ngamcharussrivichai, C.; Prasassarakich, P. Highly active MoS$_2$, CoMoS$_2$ and NiMoS$_2$ unsupported catalysts prepared by hydrothermal synthesis for hydrodesulfurization of 4, 6-dimethyldibenzothiophene. *Catal. Today* **2008**, *130*, 14–23. [CrossRef]

75. Escobar, M.C.; Barrera, J.A.; De los Reyes, J.A.; Toledo, V.; Santes, J.A. Colín, Effect of chelating ligands on Ni-Mo impregnation over wide-pore ZrO$_2$-TiO$_2$. *J. Mol. Catal. A Chem.* **2008**, *278*, 33–40. [CrossRef]

76. González-Cortés, S.L.; Xiao, T.C.; Costa, P.M.; Fontal, B.; Green, M.L. Urea–organic matrix method: An alternative approach to prepare Co-MoS$_2$/γ-Al$_2$O$_3$ HDS catalyst. *Appl. Catal. A Gen.* **2004**, *270*, 209–222. [CrossRef]

77. González-Cortés, S.L.; Xiao, T.C.; Rodulfo-Baechler, S.M.; Green, M.L. Impact of the urea–matrix combustion method on the HDS performance of Ni-MoS$_2$/γ-Al$_2$O$_3$ catalysts. *J. Mol. Catal. A Chem.* **2005**, *240*, 214–225.

78. Bin, L.I.U.; Lei, L.I.U.; Chai, Y.M.; Zhao, J.C.; Liu, C.G. Essential role of promoter Co on the MoS$_2$ catalyst in selective hydrodesulfurization of FCC gasoline. *J. Fuel Chem. Technol.* **2018**, *46*, 441–450.

79. Li, X.; Bai, J.; Wang, A.; Prins, R.; Wang, Y. Hydrodesulfurization of dibenzothiophene and its hydrogenated intermediates over bulk Ni$_2$P. *Top. Catal.* **2011**, *54*, 290–298. [CrossRef]

80. García-Martínez, J.C.; Dutta, A.; Chávez, G.; De los Reyes, J.A.; Castillo-Araiza, C.O. Hydrodesulfurization of dibenzothiophene in a micro trickle bed catalytic reactor under operating conditions from reactive distillation. *Int. J. Chem. React. Eng.* **2015**, *14*, 769–783. [CrossRef]

81. Torres-García, N.L.; Huirache-Acuña, R.; Zepeda-Partida, T.A.; Pawelec, B.; Fierro, J.L.G.; Vázquez-Salas, P.J.; Maya-Yescas, R.; Rivera-Garnica, J.M. Trimetallic Ru$_x$MoNi catalysts supported on SBA-15 for the hydrodesulfurization of dibenzothiophene. *Int. J. Chem. React. Eng.* **2019**, *17*, 2194–5748. [CrossRef]

82. Li, M.; Song, J.; Yue, F.; Pan, F.; Yan, W.; Hua, Z.; Li, L.; Yang, Z.; Li, L.; Wen, G.; et al. Complete Hydrodesulfurization of Dibenzothiophene via Direct Desulfurization Pathway over Mesoporous TiO$_2$-Supported NiMo Catalyst Incorporated with Potassium. *Catalysts* **2019**, *9*, 448. [CrossRef]

83. Li, X.; Wang, A.; Wang, Y.; Chen, Y.; Liu, Y.; Hu, Y. Hydrodesulfurization of dibenzothiophene over Ni-Mo sulfides supported by proton-exchanged siliceous MCM-41. *Catal. Lett.* **2002**, *84*, 107–113. [CrossRef]

84. Liu, X.; Liu, J.; Li, L.; Guo, R.; Zhang, X.; Ren, S.; Guo, Q.; Wen, X.-D.; Shen, B. Hydrodesulfurization of dibenzothiophene on TiO$_2$−x-modified Fe-based catalysts: Electron transfer behavior between TiO$_2$−x and Fe species. *ACS Catal.* **2020**, *10*, 9019–9033. [CrossRef]